Aberrant axonal pathfinding and exuberant myelination in an inducible model of neocortical heterotopia

Authors: Alice M. Li[1,3], Robert A. Hill[2,3*], and Jaime Grutzendler[1,3,4*]

[1] Interdepartmental Neuroscience Program, Yale School of Medicine, New Haven, CT, 06520, USA.

[2] Department of Biological Sciences, Dartmouth College, Hanover, NH, 03755, USA.

[3] Department of Neurology, Yale School of Medicine, New Haven, CT, 06520, USA.

[4] Department of Neuroscience, Yale School of Medicine, New Haven, CT, 06520, USA.

*Correspondence: robert.hill@dartmouth.edu; jaime.grutzendler@yale.edu

ABSTRACT

Neocortical heterotopia consist of ectopic neuronal clusters that are frequently found in individuals with cognitive disability and epilepsy. However, their pathogenesis remains poorly understood due in part to a lack of tractable animal models. We have developed an inducible model of focal heterotopia that enables their precise spatiotemporal control and high-resolution optical imaging in live mice. Here we report that heterotopia are associated with striking patterns of hypermyelinated and circumferentially projecting axons around neuronal clusters. Despite their aberrant axonal patterns, *in vivo* calcium imaging revealed that heterotopic neurons remain functionally connected to other brain regions, highlighting their potential to influence global neural networks. These aberrant patterns only form when heterotopia are induced during a critical embryonic temporal window, but not in early postnatal development. Our model provides a new way to investigate heterotopia formation *in vivo* and revealed features suggesting the existence of developmentally-modulated, neuron-derived axon guidance and myelination factors.

INTRODUCTION

Up to one third of routine postmortem examinations reveal the presence of neocortical heterotopia[1–4], a heterogeneous group of focal cortical lamination defects characterized by abnormally positioned clusters of neurons[5,6]. Heterotopia have been linked to many neurological conditions including epilepsy, intellectual disability, and dyslexia[3,7–12]. However, comprehensive exploration of their pathogenesis and pathophysiology has been limited by a lack of tools for their investigation in the live animal. Several genetic, traumatic, chemotoxic and other neocortical heterotopia models have been described[13–21]. However, these previous models have not been utilized for cellular intravital optical imaging analyses largely due to the lack of control over the position and timing of heterotopia induction and/or limited means for targeted cell labelling.

Here, we developed a methodology enabling the specific induction and visualization of focal heterotopia in the live mammalian neocortex. Our model uses *in utero* electroporation[22–24] combined with *in vivo* optical imaging, to generate and track layer I cortical heterotopia. When visualized using label free myelin imaging[25–27], we identify striking patterns of aberrantly projecting and hypermyelinated axons surrounding the heterotopic neurons. These distinct patterns emerge only when the heterotopia are induced during a critical embryonic period, suggesting the presence of locally-derived, developmentally-modulated signals that initiate the abnormal structural organization and myelination of the heterotopic axons. Identification and characterization of the neuronal and glial subtypes within the induced heterotopia revealed many consistent features that are used to define spontaneously occurring heterotopia in both humans[28,29] and rodent models[18,30–33]. Finally, using genetically encoded calcium biosensors, we reveal that heterotopic neurons display similar calcium transient frequencies as neighboring layer II/III neurons and respond to sensorimotor stimulation in behaving mice, opening new possibilities for the exploration of their influence on cortical function.

49 **RESULTS**

50

51 **Spatiotemporally precise layer I heterotopia generation and visualization in the live mouse**
52 **brain**

53 *In utero* electroporation (IUE) is a powerful technique that permits labeling and genetic
54 manipulation of targeted cortical neurons[22–24]. As part of the IUE procedure, a thin glass
55 microcapillary needle is used to deliver genetic material into the lateral ventricle of embryonic
56 stage animals for the electroporation of neuronal progenitors (Fig. 1a). While implementing IUE
57 to label and image cortical axons *in vivo*, we unexpectedly found that cortical sites that had been
58 injected during the procedure developed marked accumulations of labelled neuronal cell bodies
59 in layer I of adult mice (Fig. 1c, top row). Electroporated pyramidal cells are normally found in
60 layers II/III of cortical regions, thus their distinct presence at injected layer I sites stood out in
61 contrast to non-injected surrounding cortical areas (Fig. 1c, top row). *In vivo* labeling of neurons
62 with a fluorescent dye called NeuO[34] further revealed that the IUE-labelled neuronal cell bodies
63 constituted only a small fraction of the total neuronal cell bodies ectopically positioned (Fig.1b, c;
64 for detailed statistics see Supplementary File 1; mean diameter of $NeuO^+$ ectopic cell clusters 474
65 ± 174 µm s.d. in n = 23 mice). Abnormal superficial clustering of neuronal cell bodies is a defining
66 feature of layer I heterotopia[1,4,28], a subtype of neocortical heterotopia that has been linked to
67 learning impairments in humans[7,35,36]. Their presence demonstrates that direct injections into the
68 cortex performed as part the IUE procedure can induce molecularly tractable neocortical
69 heterotopia *in vivo.*

70

71 **Aberrant axonal and myelin patterns characterize layer I heterotopia formed during a**
72 **critical embryonic time window.**

73 Using this methodology, we set out to examine the cellular composition of the layer I
74 heterotopia. Interestingly, we observed markedly aberrant patterns of myelinated axons

exclusively associated with the ectopic neuronal clusters (Fig. 2a and Fig. 3a), as visualized *in vivo* by spectral confocal reflectance microscopy (SCoRe), a technique that enables high resolution label-free imaging of myelinated axons[25,26]. This was further corroborated by fixed tissue immunohistochemistry of myelin markers, showing increased oligodendrocyte and myelin densities at the sites of injection (Fig. 2b-d, Fig. 3e-g, and Figure 3–figure supplement 1; for detailed statistics see Supplementary File 1). On closer examination *in vivo*, we observed both myelinated and unmyelinated axons swirling in a nest-like fashion around heterotopic neurons (Fig. 2a, Fig. 3a-d, and Figure 3–figure supplement 1), often forming thick concentric borders that were most prominent towards the pial surface (Fig. 3e-g and Video 1). Radially-oriented, myelinated fiber bundles were also observed projecting out from underneath the heterotopia (Fig. 2b-c and Figure 2–figure supplement 1), similar to previous descriptions of spontaneously occurring layer I heterotopia[28–31]. Thus, by applying our methodology in combination with SCoRe microscopy and immunohistochemical analyses, we discovered that distinct axon guidance and myelin abnormalities occur in embryonically-induced layer I heterotopia.

To investigate whether the marked axonal and myelin changes were dependent on induction of heterotopia at specific developmental ages, we performed IUE at various time points during cortical development between embryonic day 14 (E14) to E17, and postnatal day 0 (P0). We found that whereas embryonic injections always resulted in similar nest-like patterns of densely myelinated fiber bundles around heterotopic neurons (Fig. 4, Fig. 5b), P0 injections did not result in robust axon guidance or myelination abnormalities, despite the presence of ectopic neural clusters (Fig. 5a). Although postnatally-induced heterotopia tended to be smaller and more variable in size (data not shown), the axonal and myelin abnormalities were never observed even around larger P0-induced clusters (Fig. 5a). Consistent with this, we found no significant difference in the myelin or oligodendrocyte cell body densities (Fig. 5c; for detailed statistics see Supplementary File 1) between heterotopia and contralateral control regions of P0-injected mice. Likewise, immunolabelling for neurofilament heavy chain (NF-H) did not reveal aberrant

accumulations of axonal fibers (Fig. 5a). Together, our data indicate previously unrecognized differences in the cellular composition and organization of neocortical heterotopia based on the timing of their induction.

Astrocyte and microglia cell densities are not altered in induced heterotopia

Given the striking abnormalities in oligodendrocyte production, myelination and axon pathfinding observed in the embryonically-induced heterotopia, we next wondered whether other glial cell types such as astrocytes and microglia also exhibited altered morphology or density. Immunolabelled cortical brain sections against Aldh1L1 revealed no significant difference in the astrocyte cell density between layer I heterotopia and corresponding contralateral control regions (Fig. 6a-c; for detailed statistics see Supplementary File 1). Similarly, using Iba1 immunolabelling, we found no regional differences in microglia density or morphology (Fig. 6d-f; for detailed statistics see Supplementary File 1). Moreover, there was no evidence of pronounced astrocytic or microglial accumulation or altered cellular morphology at the borders of the heterotopia suggesting that a glial scar had not formed due to the embryonic injection. These data suggest that while heterotopia induce marked oligodendrocyte generation, astrocytes and microglia are not significantly influenced by potential local factors derived from ectopic neuronal clusters.

Heterotopia contain a variety of excitatory and inhibitory neurons born at different embryonic ages

To characterize the neural composition of the induced heterotopia, we examined the expression of neuronal subtype markers Cux1, Tle4, and GAD-67 (Fig. 7). Cux1 is a transcription factor predominantly expressed in callosal projection neurons in layers II-IV[37], whereas Tle4 is primarily restricted to deeper corticothalamic projection neurons of layers V and VI[38,39]. We found both Cux1^{+} and Tle4^{+} neurons present to varying degrees in all layer I heterotopia (Fig. 7b, c and Figure 7–figure supplement 1), consistent with a mixed population of excitatory projection neurons

127 from different cortical layers. Further analyses revealed the presence of GAD67$^+$ interneurons,
128 which occurred at similar densities within heterotopia as in corresponding layer I control regions
129 (Fig. 7d-f; for detailed statistics see Supplementary File 1). In addition, layer I heterotopia always
130 contained GAD67$^+$ puncta, consistent with inhibitory synapses (Fig. 7d, e). Together, our findings
131 suggest that induced layer I heterotopic neural clusters comprise a diverse cohort of glutamatergic
132 and GABAergic neurons, in line with the heterogeneous population of neuronal subtypes
133 previously described in those occurring spontaneously[31,33,40,41].

134 We next used birthdating techniques to determine whether neurons within the induced
135 heterotopia originate at similar or different time points during development. 5-Ethynyl-2´-
136 deoxyuridine (EdU) pulse labelling at E11.5 revealed small but distinct populations of EdU$^+$NeuN$^+$
137 cells in all embryonically-generated layer I heterotopia (Figure 7–figure supplement 2), suggesting
138 that heterotopia contain neurons born during early corticogenesis[42,43]. We also observed cells
139 "birthdate-labelled" via IUE[22] at E15 (~90% heterotopia in n > 30 mice; Fig. 1c) in heterotopia,
140 suggesting the additional presence of later-born neurons. These data indicate that induced
141 heterotopia contain neurons born at various stages of cortical development.

142

143 **Heterotopic neurons exhibit similar calcium dynamics as neighboring normotopic neurons**

144 Despite their linkage to a wide spectrum of neurological disorders, the cellular dynamics
145 and mechanisms by which individual heterotopic cells contribute to neural circuit dysfunction are
146 poorly understood. We examined the calcium activity of single cortical neurons in induced
147 heterotopia and in surrounding, non-injected cortical layer II/III regions of awake head-fixed mice
148 using the genetically encoded calcium indicator, GCaMP6f. Surprisingly, although we found highly
149 variable calcium spike patterns of individual cells within heterotopia (Fig. 8a-c and Video 2), there
150 were no significant differences in their overall calcium spike event frequency, variance, or
151 synchrony compared to surrounding non-heterotopic layer II/III regions (Fig. 8d; for detailed
152 statistics see Supplementary File 1). Furthermore, we did not identify any epileptiform activity in

our imaging sessions, although we cannot rule out that continuous recordings could have revealed sporadic aberrant activity (Fig. 8a-c and Video 2). Interestingly, we found that mice that had been startled with brief whisker stimulation consistently responded via neuronal calcium spikes within layer I heterotopia (Fig. 8e, f and Video 3). This result indicates that heterotopic neurons are connected to other brain areas and could thus influence network function.

158 **DISCUSSION**

159

160 Here we describe an inducible model that allows the visualization of focal heterotopia at
161 cellular resolution in the live animal. By mechanically puncturing the cortex as part of the IUE
162 procedure we induce a targeted layer I heterotopion that can be repeatedly imaged *in vivo*. Pairing
163 this methodology with intravital fluorescence and label-free (SCoRe) microscopy of neuronal cell
164 bodies, axons and myelin, as well as time lapse axonal and calcium imaging[22,23,25,34,44], enables
165 detailed studies of heterotopia in the intact brain.

166 Many animal models of focal heterotopia have been described however most involve
167 subcortical or intrahippocampal heterotopia[13,14,17,19,45], which are not easily amenable to intravital
168 optical imaging due to their distance from the cortical surface. Moreover, other animal models of
169 more superficially-occurring heterotopia[15,16,18,21,46] have not been imaged successfully at high
170 resolution *in vivo* mainly as a result of their temporally and spatially unpredictable nature and/or
171 lack of visible cell transfection. Our methodology improves upon these limitations by employing
172 minimally invasive microinjections to both induce layer I heterotopia and deliver plasmid DNA or
173 viral vectors for cellular genetic manipulation in the live mouse.

174 Using our model, we revealed several striking characteristics of neocortical heterotopia.
175 First, we discovered that axonal projections within layer I heterotopia formed swirled and
176 concentric morphologies specifically around heterotopic neuronal clusters. Interestingly there was
177 no evidence of glial scarring or mechanical tissue barriers surrounding the heterotopia, suggesting
178 that the directional changes in axon pathfinding were instead likely mediated by disruptions in the
179 precise balance of repulsive and attractive gradients of local axon guidance cues[47–51]. These axon
180 pathfinding abnormalities led us to investigate whether the developmental timing of heterotopia
181 induction could modulate their formation. We found that whereas embryonically-induced
182 heterotopia always displayed distinct axon guidance abnormalities, similar defects were not

183 observed in postnatally-induced heterotopia. This surprising finding suggested the presence of a
184 critical gestational time period during which cortical axon pathfinding is uniquely sensitive to local
185 environmental disturbances. The distinct responsiveness of axons during this critical period could
186 be mediated by the enhanced expression of axon growth cone receptors that increase the ability
187 of axons to extend toward guidance cues[52,53]. However, developmentally modulated changes in
188 the signaling gradients of guidance cues themselves could also play a role[54].

189 In addition to aberrant axonal organization, we used label-free SCoRe *in vivo* imaging to
190 discover restricted hypermyelination specifically within the heterotopia. This focal
191 hypermyelination was due to an increased production of myelinating oligodendrocytes that
192 deposited myelin sheaths primarily along the aberrantly projecting and concentric axons.
193 Interestingly, the hypermyelination was only observed in embryonically-induced but never in
194 postnatally-induced heterotopia. Similar to the critical period for disrupted axonal patterning, these
195 data suggest that the myelination of embryonically-induced heterotopia is instructed by
196 developmentally regulated molecules or biophysical cues, which could accelerate the local
197 production of myelin by stimulating oligodendrocyte precursor cell recruitment and/or
198 differentiation. Myelin formation is influenced by axon caliber[55] and genetic manipulations
199 increasing axon caliber can trigger oligodendrocyte precursor cell proliferation and the
200 ensheathment of classically unmyelinated fibers[56]. Thus, axon caliber could serve as one
201 mechanism that differs between the aberrantly projecting axons found in embryonically-induced
202 heterotopia compared to adjacent non-myelinated cortical axons. Other potential causes for the
203 localized hypermyelination of heterotopic axons could include cell surface markers or molecular
204 identity. Specific subpopulations of excitatory[57] and inhibitory[58] neurons exhibit variable
205 myelination patterns, seemingly not directly linked to axon caliber, but instead potentially due to
206 their differential expression of adhesion molecules or altered patterns of neuronal activity. Our
207 model provides a novel means to test these possibilities in future studies.

208 Despite the striking axon and myelin abnormalities associated with the induced
209 heterotopia, we found no evidence of spontaneous epileptiform activity occurring in heterotopic
210 regions or nearby non-heterotopic cortices of awake animals, consistent with previous
211 studies[40,59,60]. Moreover, spontaneous calcium fluctuations and relative synchrony of firing
212 between neurons in layer I heterotopia and neighboring layer II/III cortex were similar. This lack
213 of observable difference in activity may reflect the similar neural composition of both brain areas,
214 which could enable a similar balance of excitatory and inhibitory inputs to these regions. Indeed,
215 we identified Cux1^{+} cells, GABAergic neurons and GABAergic puncta in layer I heterotopia that
216 are also prevalent in layers II/III[37,61–63]. A second, non-mutually exclusive possibility is that more
217 metabolically demanding conditions are required to trigger aberrant activity in mice with induced
218 heterotopia. Consistent with this hypothesis, the application of normally subthreshold doses of
219 convulsant drugs can provoke epileptiform activity in mice with heterotopia *in vitro*[64] and *in*
220 *vivo*[59,64,65]. Other animal models of heterotopia, such as the *tish* mutant[13] and Ihara's genetically
221 epileptic rat[19] have documented spontaneous epileptiform activity *in vivo*. Reasons for this
222 difference from our findings remain unclear, however they may be related to disparities in the
223 number, location or size of heterotopia, or unknown off-target effects of the inherited mutations
224 themselves in the genetic models.

225 There is little known about the functional dynamics of individual heterotopic neurons during
226 behavioral stimulation in the live animal. Using time-lapse calcium imaging, we revealed that
227 heterotopic neurons display robust responses following brief whisker stimulation in awake mice,
228 consistent with the functional connectivity implicated by previous anatomical, electrophysiological,
229 and behavioral studies[13,40,59,66–69]. This functional connectivity suggests that, even though we did
230 not detect aberrant spontaneous activity within heterotopia, these neurons are integrated into the
231 local neural network and are potentially capable of altering neural network function at baseline or
232 under metabolically demanding conditions.

233 We describe an inducible model of heterotopia amenable to intravital visualization that
234 closely mimics the neural, glial, axonal, and myelin profiles of those occurring spontaneously in
235 layer I[28,33]. Building upon previous models, this system employs *in utero* microinjections to directly
236 provoke the disruptions in pial basement membrane and radial glial scaffolding thought to
237 culminate in the neural migration defects leading to their development[70]. Importantly, this model
238 allows imaging of the downstream effects of this disruption using multiple optical, functional, and
239 molecular probes for different cell subtypes[22,23,25,34,44], adding a powerful new tool for the study of
240 cortical malformations in the live mammalian brain.

241 **MATERIALS AND METHODS**

242

243 *Animals*

244 All experimental approaches and procedures were conducted in accordance with Yale
245 University Institutional Animal Care and Use Committee regulations. Timed pregnant outbred
246 CD1 mice were purchased from Charles River Laboratories, Inc, with the first 24 hours of
247 postnatal life designated as P0. We included both male and female mice, aged to P30 – P60, for
248 this study. For some birth dating experiments as described in the text, pregnant dams were given
249 a single intraperitoneal (i.p.) injection of EdU (30 µg g^{-1} body weight) at E11.5, prior to IUE surgery
250 at E15. Litters were kept in individual ventilated cages until weaning age (P21), after which mice
251 were housed in single-sex groups with 2 – 5 animals per unit. Cages were maintained in
252 temperature-controlled facilities with 12-hour light/12-hour dark cycles.

253

254 *In utero intracranial injection, electroporation and viral infection*

255 Embryonic cortical injections were performed as part of the IUE procedure during needle
256 insertion into the lateral ventricle[23,71]. Embryos were injected once unilaterally
257 between embryonic day 14 – 17 (E14 - E17) for all electroporations, as specified in the
258 text. Intracranial injections were not performed at gestational ages below E14 or over E17 due to
259 the technical challenges associated with maintaining embryo viability. To
260 keep consistent experimental design parameters, however, all quantifications for *in vivo* and
261 fixed tissue analyses used only E15-injected embryos.

262 All *in utero* injections were targeted toward prospective somatosensory cortices.
263 Injection solutions included the following plasmid and viral components for neuronal
264 labelling: pCAG-tdTomato (based on Addgene plasmid 11150) and rAAV8-hSyn-eGFP (UNC
265 Vector Core, Lot AV5075D; titer 3.9e12 GC ml^{-1}). Injection solutions contained either pCAG-
266 tdTomato (1.5 µg $µL^{-1}$ final concentration) only, or both pCAG-tdTomato (1.5 ug $µl^{-1}$ final

concentration) and AAV8-hSyn-eGFP (final titer 3.9e11 GC ml^{-1}) in saline solution. All injection solutions contained Fast Green FCF dye (TCI; 2 mg ml^{-1}) to facilitate their visual tracking during the injection procedure. Procedures for *in utero* electroporation have been previously described[23,71]. Briefly, timed pregnant CD1 dams were anesthetized with a saline solution containing both ketamine (100 - 120 mg kg^{-1}) and xylazine (10 - 12 mg kg^{-1}), delivered i.p. Following induction of deep surgical anesthesia, midline incisions (1¼ inch) were made into the abdominal skin and muscle wall to access the underlying uterus. Pulled glass capillary needles (10 µL Drummond Scientific Glass Capillaries, Cat# 3-000-210-G; pulled to ~ 50 µm diameter at tip and ~ 125 µm diameter at 1mm above tip) were then used to puncture the uterine wall and deliver (Picospritzer II, General Valve) 0.5 µl of injection solution into the lateral ventricle of individual embryos. Each embryo was injected only once and subsequently electroporated using BTX tweezertrodes aimed at the somatosensory cortex of the injected hemisphere. All electroporations were conducted using four 50 ms, 50 V electrical pulses, delivered at 1 second intervals (BTX Harvard Apparatus 8300 pulse generator).

Postnatal intracranial viral injection

Intracranial injections were performed on P0 pups from timed pregnant CD1 dams that were naïve to the *in utero* electroporation procedure. Injection solutions included one of the following viruses to mark injected regions: rAAV8-hSyn-eGFP (UNC Vector Core, Lot AV5075D; titer 3.9e12 GC ml^{-1}) and rAAV2-CaMKIIa-mCherry (UNC Vector Core, Lot AV4377d, 3.8e12 titer GC ml^{-1}). P0 intracranial injections were performed essentially as previously described[72]. Briefly, neonates were cryoanesthetized[73] within 24 hours following birth. After confirming loss of voluntary movement, neonates were placed in the prone position on a polymer cooling block. A pulled glass capillary needle (10 µl Drummond Scientific Glass Capillaries, Cat# 3-000-210-G; pulled to ~ 75 µm diameter at tip and ~ 325 µm diameter at 4 mm above tip), advanced 4mm past the dorsal scalp at a 90° angle, was then used to deliver into the brain parenchyma 1 µl of virus

293 solution (diluted 1:10 in PBS and 2 mg ml^{-1} Fast Green FCF, TCI from stock). Each neonate
294 received only one unilateral intracranial injection targeted over somatosensory cortices. Injected
295 neonates were then rewarmed on a heating pad and placed back with their biological mother. All
296 P0-injected mice were sacrificed for analysis at P30, with quantifications and analyses performed
297 in fixed tissue to circumvent the obstructive meningeal scarring and parenchymal adhesions
298 associated with P0-injections on *in vivo* imaging.
299

300 *Postnatal subarachnoid viral injection*

301 Injection solutions were prepared using AAV9-Syn-GCaMP6f-WPRE-SV40 (Penn Vector
302 Core, Lot CS1001; titer 7.648e13 GC ml^{-1}) virus diluted 1:100 in PBS and Fast Green FCF (TCI;
303 2 mg ml^{-1}). P21- P30 mice that had previously been electroporated *in utero* were anesthetized by
304 intraperitoneal injections of ketamine (100 mg kg^{-1}) and xylazine (10 mg kg^{-1}). The scalp was
305 shaved, cleaned, and then incised to expose the underlying bone. A high speed drill was next
306 employed to introduce a small burr hole (~ 0.75 mm diameter) over the transfected hemisphere,
307 taking care to avoid cortical regions suspected to have been directly punctured as part of the *in*
308 *utero* electroporation procedure. The underlying dura was gently detached, and a 12 µL volume
309 of injection solution (prepared as described above) was infused into the subarachnoid space to
310 achieve viral transfection of both layer I heterotopic and layer II/III neurons via topical cortical
311 application. The scalp incision was then closed with sutures. Cranial windows for *in vivo* imaging
312 were prepared over injected cortical hemispheres 3 – 4 weeks following the subarachnoid AAV
313 infusion.
314

315 *Cranial window surgery and in vivo imaging*

316 All *in vivo* imaging was performed using cranial windows[26]. Briefly, mice were
317 anesthetized using ketamine (100 mg kg^{-1}) and xylazine (10 mg kg^{-1}), delivered via i.p. injection.
318 The dorsal skull surgical field was shaved and cleaned, and a ~4 mm diameter circular region of

319 skull and dura mater was excised from the injected hemisphere. A #0 transparent glass coverslip
320 was then gently implanted on top of uncovered pial surface to serve as the cranial window. Glue
321 and dental cement were applied to secure the window to surrounding skull bone.

322 To detect neuronal cell bodies *in vivo* as described in the text, the fluorescent membrane-
323 permeable probe NeuO (NeuroFluor, Stemcell Technologies Cat# 01801, diluted 1:25 in PBS)
324 was applied to exposed cortex for 20 min followed by a 1-2 min PBS rinse, before the placement
325 of the #0 glass coverslip during the cranial window surgery. In some cases, 100 µL Evans blue
326 (TCI; 1 mg ml^{-1}) was injected intravenously after the cranial window surgery to label the cortical
327 vasculature.

328 Except for GCaMP6f calcium imaging experiments, all *in vivo* imaging studies used mice
329 that were anesthetized via i.p. ketamine and xylazine injection. *In vivo* imaging of anesthetized
330 mice was performed at P30 immediately after cranial window surgery. All
331 intravital GCaMP6f calcium imaging was carried out in P50 - P60 awake head-fixed mice starting
332 four hours after arousal from cranial window surgical anesthesia.

333 Confocal *in vivo* images of previously injected cortical areas with or without the needle
334 tract sites were acquired using a 20X water immersion objective (Leica, 1.0 NA) on a Leica SP5
335 upright laser scanning microscope. Spectral confocal reflectance (SCoRe) imaging to detect
336 myelinated axon segments was performed as previously described[25,26] by capturing the
337 simultaneously reflected light signals from 488 nm, 561 nm, and 633 nm multi-wavelength laser
338 excitation outputs. Single-photon laser outputs were tuned to the following excitation wavelengths
339 for fluorescence imaging: 488 nm for GFP and NeuO; 561nm for tdTomato and mCherry; 633nm
340 for Evans Blue. Sequential imaging was employed to minimize overlap between SCoRe reflection
341 and individual fluorescence emission signals for all *in vivo* confocal imaging experiments.

342 Needle tracts from injections performed *in utero* were identified by the abrupt changes in
343 orientations of labelled dendritic and axonal processes around breaks in the cortical surface *in*
344 *vivo*. Since needle tracts identified in this manner always displayed ectopic neural clusters of

similar expanse in layer I, the outer boundaries of 'heterotopia' *in vivo* were defined as the layer I needle tract borders for all quantifications. Ipsilateral, non-injected cortical areas were defined as layer I regions at least 150 μm away from a discernable injection site border. Heterotopia and ipsilateral control regions were imaged using identical laser output and image acquisition configurations that were determined for each experimental data set. Confocal z-stacks were acquired at 1024 × 1024 pixel resolution starting from the pia through depths of up to 120 μm below the cortical pial surface. In some cases, time lapse imaging of *in utero*-induced heterotopia was also performed at 512 X 512 pixel resolution.

For some GCaMP6f calcium imaging experiments that involved visualization of deeper cortical regions in layers II/III as indicated in the text, time-lapse fluorescence images were acquired using a 20X water immersion objective (Zeiss, 1.0 NA) on a Prairie Technologies two-photon microscope fitted with a mode-locked, tunable Spectra Physics Mai-Tai laser. In these experiments, the two-photon laser was tuned to 920nm for excitation of both GCaMP6f and TdTomato fluorophores. All two-photon time-lapse imaging was performed at 512 X 512 pixel resolution.

In vivo image processing and quantification

Except for GCaMP6f calcium imaging experiments which were conducted using P50 - P60 mice, all intravital imaging studies were performed using P30 mice, with quantifications carried out on those that had previously been injected at E15. All *in vivo* images were processed and quantified using ImageJ/FIJI.

For SCoRe density quantifications, we analyzed single z-sections located 10 μm deep to the cortical pial surface from both heterotopic and ipsilateral control regions. SCoRe density values were assessed using a custom-built, automated thresholding and binarization macro in Image/FIJI, with Robust Automatic Threshold parameters set to noise = 25, lambda = 3, min = 31. Randomly selected, equally sized regions of interest (ROIs) were used to

371 determine SCoRe density values within the centers and edges of the heterotopia versus
372 control regions. A 'heterotopion center' was defined as the circular region with a radius extending
373 from the needle tract center to 1/3 of the radius of the needle tract. A 'heterotopion edge'
374 was defined as the needle tract concentric circular region just outside the 'heterotopion center',
375 extending from the 'heterotopion center' outer edge to the outermost border of the needle tract.
376 Average SCoRe densities were determined for the heterotopion center, heterotopion edge and
377 control area for each mouse (n = 8 mice). Statistical analyses were carried out using Wilcoxon
378 matched pairs, signed-rank non-parametric tests.

379 For NeuO dye-labelled cell body density quantifications, data were analyzed from the first
380 75 μm of cortex deep to the pial surface of both heterotopic and control regions in layer I. Equal-
381 sized volumes (50 μm^3) were randomly selected from the superficial cortical z-stacks captured
382 from both heterotopic and control regions. The number of $NeuO^+$ cell bodies was manually
383 counted in each volume. Average $NeuO^+$ cell body densities were then determined for
384 the heterotopic and control region of each mouse (n = 6 mice). Statistical analyses were
385 performed using Wilcoxon matched pairs, signed-rank non-parametric tests.

386 For quantification of neuronal calcium dynamics in heterotopia vs. adjacent non-injected
387 cortical areas, we used the two-photon microscope to capture 150 X 150 μm field of view
388 (FOV) time lapse images from both layer I heterotopia and non-injected ipsilateral layer
389 II/III regions. Time lapse imaging (512 X 512 pixel resolution; 2Hz) was performed in awake,
390 head-fixed mice during a 2-hour time window that started 4 hours after their arousal from cranial
391 window surgical anesthesia. For heterotopic regions, FOVs were randomly selected from within
392 the first 75 μm below the cortical surface in layer I. For layer II/III regions, FOVs were randomly
393 selected from between 120 to 175 μm below the cortical surface. Six to eight separate FOVs
394 (exactly half from layer I heterotopia and half from ipsilateral layer II/III regions) were imaged in
395 each mouse, with each FOV recorded for 120s per trial for three trials. The order in which FOVs
396 were acquired from heterotopia and layer II/III regions was alternated between mice. Time series

397 analyses were performed using ImageJ/FIJI. Prior to quantifications, TurboReg plugin in
398 ImageJ/FIJI was used to align all time series images in the XY plane.

399 To quantify GCaMP6f fluorescence changes in individual cells, ROIs were manually
400 selected to encapsulate neuronal cell bodies. GCaMP6f$^+$ cell bodies that exhibited tdTomato
401 labelling from the IUE procedure were excluded from all analyses. Approximately 10 - 25
402 GCaMP6f$^+$ cells were analyzed in each FOV. Baseline GCaMP6f fluorescence intensity values
403 (F) for each cell were defined in each trial as the average of the lowest 20% of the recorded values
404 per trial, with fluctuations from this baseline denoted as $\Delta F/F$. A spike event was defined in each
405 trial as a $\Delta F/F > 0.5$. Spike event frequencies were averaged across 3 trials for each cell in both
406 layer I heterotopia and layer II/III regions for $n = 7$ mice. Statistical analyses were performed using
407 Wilcoxon matched pairs, signed-rank non-parametric tests.

408 For quantifications of the global synchronization index reflecting the relative coordination
409 of GCaMP6f activity, analyses were performed using Fluorescence Single Neuron and Network
410 Analysis Package (FluoroSNNAP)[74]. Briefly, this semi-automated software implements a
411 correlation matrix-based algorithm[74–76] to compute the normalized global synchronization indices
412 (ranging in value from 0 to 1) for time series calcium imaging data of neural populations. The
413 highest value, 1, signifies entirely synchronized firing throughout an identified cluster of neurons,
414 whereas 0 indicates the total absence of synchrony. Synchronization cluster analyses were
415 performed using template-based calcium event detection parameters set to detection threshold =
416 0.85, minimum size of synchronization clusters = 2, and surrogate resampling = 20. A cluster of
417 neurons was defined as the GCaMP6f$^+$ cell population within one FOV. Global synchronization
418 indices were averaged across three trials for each FOV in both layer I heterotopia and layer II/III
419 regions for $n = 7$ mice. Statistical analyses were performed using Wilcoxon matched pairs,
420 signed-rank non-parametric tests.

421

422 *Tissue processing and immunohistochemistry*

423 At P30, mice were deeply anesthetized using ketamine and xylazine, and then perfused
424 transcardially with 4% paraformaldehyde in phosphate buffered saline (PBS). Harvested brains
425 were post-fixed overnight using the same solution at 4 °C, and then vibratome sectioned (coronal;
426 75 μm thickness) for fixed tissue analysis.

427 To identify brain regions that had been injected as part of the IUE procedure, a
428 fluorescence microscope was next used to examine the sections for visibly disrupted layer I
429 regions showing transfected neurons and/or neuronal processes, similar to what has been
430 previously described[46]. The disrupted regions often revealed cellular clusters
431 containing $eGFP^+$ neurons that protruded past the pial surface, which were never observed in
432 intact cortical regions or in non-injected mice. Sections containing visibly disrupted layer I cortical
433 cytoarchitecture indicative of injection-associated trauma were then selected for further
434 processing. Immunohistochemistry, performed as described below, was used to confirm the
435 presence of layer I heterotopia at all identified IUE injection sites. Coronal sections from P0-
436 injected mice were screened in a similar manner for injected areas, which were identified by virally
437 transfected axonal fibers and neuronal cell bodies concentrated around visible needle tracts (data
438 not shown).

439 Prior to immunostaining, all free-floating sections were heated to 95 °C for 30 minutes in
440 50 mM sodium citrate buffer (0.05% Tween-20, pH 6.0) for antigen retrieval and elimination of
441 endogenous eGFP expression. After rinsing the sections in PBS at room temperature, EdU
442 labelling was next carried out in some experiments as specified by the Click-iT EdU Alexa Fluor-
443 647 Imaging Kit protocol (Cat# C10340). Before proceeding to antibody staining, all tissues
444 were pre-incubated for 1-2 hr in 0.1% Triton X-100 and 5% Normal Goat Serum (NGS;
445 Jackson Immunoresearch, Cat# 005-000-121) in PBS at room temperature. Slices were then
446 incubated with primary antibody for 1.5 hrs - 2 days as needed in 0.1% Triton X-100 and 5% NGS
447 in PBS at 4 °C. The primary antibodies used were: rabbit anti-NeuN (Abcam, Cat# ab177487,
448 1:3000), mouse anti-NeuN (Abcam, Cat# ab104224, 1:1000), mouse anti- Myelin CNPase (clone

449 SMI 91, Biolegend, Cat# 836404, 1:1000), rabbit anti-Cux1 (Novus Biologicals, Cat# NBP2-
450 13883, 1:100), mouse anti-Tle4 (E-10) Alexa Fluor 647 (Santa Cruz Biotechnology, Cat# sc-
451 365406 AF647, 1:100), mouse anti- GAD-67 (EMD Millipore, Cat# MAB5406, 1:1000), rabbit anti-
452 Iba1 (Wako, Cat# 019-19741, 1:600), mouse anti-Aldh1l1 (clone N103/39, NeuroMab, Cat# 75-
453 140, 1:500), chicken anti-Neurofilament NF-H (EnCor, Cat# CPCA-NF-H, 1:500), chicken anti-
454 GFP (Abcam, Cat# 13970, 1:500), and rabbit anti-Myelin Basic Protein (MBP; Abcam, Cat#
455 40390, 1:1000). Following primary antibody incubation, slices were washed in PBS and then
456 incubated with Alexa Fluor dye-conjugated secondary antibodies of the appropriate host species
457 at 1:600 dilution in 0.1% Triton X-100 and 5% NGS in PBS for 1 - 2 days at 4 °C. After secondary
458 antibody incubation, sections were washed again in PBS and incubated with 2.5 µg mL^{-1} 4′,6-
459 diamidino-2-phenylindole (DAPI) in PBS for 15 min at room temperature to counterstain cell
460 nuclei. Following an additional subsequent wash, stained sections were mounted with 25%
461 mounting media solution (Dako Ultramount, Cat# S1964; diluted 1:4 in PBS) onto glass slides for
462 imaging.
463
464 *Fixed tissue imaging and quantification*
465 Images of stained sections were collected using a Leica SP5 upright confocal laser
466 scanning microscope. Lower magnification views of analyzed sections for presentation were
467 acquired using 10X and 20X Leica objectives. All fixed tissue images for quantification were
468 captured through a 40X Leica water immersion objective. For immunohistochemical analyses of
469 *in utero*-injected mice, 'heterotopia' were defined as the layer I cortical regions demarcated by
470 ectopic $NeuN^+$ cell body clusters identified at IUE needle tract sites. For P0-injected mice,
471 because the heterotopia associated with needle tracts were more variable in size, ranging from
472 several cells to 350 µm in diameter (data not shown), data for these injected areas were obtained
473 from 300 µm X 90 µm FOVs centered on visible needle tracts that were within the first 100 µm
474 below the pial surface. Control, non-injected regions were specified on corresponding

475 contralateral cortices at similar mediolateral distances from the midline. Identical laser output and
476 image acquisition configurations were used to capture images of both heterotopia and
477 contralateral control regions throughout each immunostaining set.

478 All data for Aldh1l1, Iba1, CNPase, and GAD-67 cell density quantifications were acquired
479 from the most superficial 100 μm of cortical tissue of both heterotopic and contralateral
480 homologous control regions in layer I. The number of cell bodies confirmed by DAPI labelling that
481 were positive for each marker was manually counted in randomly selected volumes within z-
482 stacks acquired from both regions. The volumes were kept at identical dimensions between
483 heterotopia and contralateral control regions for each experiment. For GAD-67 immunostaining,
484 the presence of neuronal cell bodies was also confirmed by NeuN labelling. Two coronal sections
485 containing heterotopia were analyzed per animal, with each immunostaining set comprising n = 6
486 animals. Statistical analyses were performed using Wilcoxon matched pairs, signed-rank non-
487 parametric tests.

488 Data for CNPase density quantifications were acquired from the most superficial 100 μm
489 of cortical tissue in both heterotopia and contralateral control regions. CNPase intensity was
490 assessed using an automated thresholding and binarization plugin in Image/FIJI (Robust
491 Automatic Threshold parameters set to noise = 1, lambda = 2, min = 208) for equally-sized ROIs
492 that were randomly selected from within heterotopic and contralateral control z-projections (15
493 μm thickness). CNPase density values for each section were determined by subtracting the
494 automated measurements made in additional background regions from those made in assessed
495 heterotopic and control regions. Two coronal sections containing heterotopia were analyzed per
496 animal (n = 6 animals). Statistical analyses were performed using Wilcoxon matched pairs,
497 signed-rank non-parametric tests.

498 To examine the neuronal composition of the embryonically-induced heterotopia, coronal
499 sections were stained for NeuN, DAPI and one of the other following stains: Cux1, Tle4,
500 or EdU as indicated in the text. Data were acquired from within the most superficial 100 μm of the

501 neocortex for layer I heterotopia, and across the entire cortical wall for contralateral homologous
502 control regions. For quantification of layer I heterotopia, equally sized VOIs were randomly
503 selected from within the first 100 μm below the pial surface. For quantification of control regions
504 on the contralateral hemisphere, the cortical wall was partitioned into 11 equal volume bins
505 extending from the pial surface to white matter, with Bin1 encompassing layer 1 and Bin 11
506 adjoining white matter at its lower boundary. For each heterotopic VOI and control bin, the 1)
507 number of $NeuN^+$ cells and 2) proportion of $NeuN^+$ cells that were also Cux1, Tle4,
508 or EdU positive was manually quantified in ImageJ. Cells were identified as EdU positive if >
509 50% of their nuclear volume, defined by DAPI, was occupied by EdU. Two sections were
510 analyzed per mouse, with sample sizes for each group denoted in the text and figure legends.

511 The sites of injection analyzed in this study were positioned in somatosensory cortices
512 and immediately adjacent areas in both male and female mice. Given the minimal variation in the
513 morphological appearances of needle tracts between male and female mice and across different
514 cortical areas, we pooled together these variables in our analyses. No animal subjects or
515 experimental data points were excluded from analysis, and the nature of our study did not require
516 subject randomization or experimenter blinding. No statistical methods were used to predetermine
517 sample sizes, although our sample sizes are comparable to those published and generally
518 accepted in the field. GraphPad Prism 7 was utilized for all statistical analyses, and Wilcoxon
519 matched pairs signed-rank non-parametric tests were used to determine statistical significance
520 (declared for p-values below 0.05; two-tailed) because a normal distribution of differences
521 between the paired data could not be assumed. Data are reported as mean ± s.e.m., unless
522 otherwise noted.

523 **REFERENCES**

524

525 1. Kaufmann WE, Galaburda AM. Cerebrocortical microdysgenesis in neurologically normal
526 subjects: a histopathologic study. *Neurology*. 1989;39(2 Pt 1):238-244.
527 doi:10.1212/WNL.39.2.238

528 2. Kasper BS, Stefan H, Buchfelder M, Paulus W. Temporal Lobe Microdysgenesis in
529 Epilepsy Versus Control Brains. *J Neuropathol Exp Neurol*. 1999;58(1):22-28.
530 doi:10.1097/00005072-199901000-00003

531 3. Meencke HJ, Veith G. Migration disturbances in epilepsy. *Epilepsy Res Suppl*. 1992;9:31-
532 39; discussion 39-40. http://www.ncbi.nlm.nih.gov/pubmed/1285910.

533 4. Schulze KD, Braak H. Hirnwarzen. *Zeitschrift fur Mikroskopisch-Anatomische Forsch -*
534 *Abteilung 2*. 1978;92(4):609-623.

535 5. Sisodiya SM. *Malformations of Cortical Development: Burdens and Insights from*
536 *Important Causes of Human Epilepsy*. Vol 3. Lancet Publishing Group; 2004:29-38.
537 doi:10.1016/S1474-4422(03)00620-3

538 6. Barkovich AJ, Gressens P, Evrard P. Formation, maturation, and disorders of brain
539 neocortex. *Am J Neuroradiol*. 1992;13(2):423-446.
540 http://www.ncbi.nlm.nih.gov/pubmed/1566709.

541 7. Galaburda AM, Kemper TL. Cytoarchitectonic abnormalities in developmental dyslexia: a
542 case study. *Ann Neurol*. 1979;6(2):94-100. doi:10.1002/ana.410060203

543 8. Hardiman O, Burke T, Phillips J, et al. Microdysgenesis in resected temporal neocortex:
544 incidence and clinical significance in focal epilepsy. *Neurology*. 1988;38(7):1041-1047.
545 doi:10.1212/wnl.38.7.1041

546 9. Palmini A, Andermann F, Olivier A, Tampieri D, Robitaille Y. Focal neuronal migration
547 disorders and intractable partial epilepsy: Results of surgical treatment. *Ann Neurol*.
548 1991;30(6):750-757. doi:10.1002/ana.410300603

549 10. Kakita A, Hayashi S, Moro F, et al. Bilateral periventricular nodular heterotopia due to
550 filamin 1 gene mutation: Widespread glomeruloid microvascular anomaly and dysplastic
551 cytoarchitecture in the cerebral cortex. *Acta Neuropathol*. 2002. doi:10.1007/s00401-002-
552 0594-9

553 11. Farrell MA, DeRosa MJ, Curran JG, et al. Neuropathologic findings in cortical resections
554 (including hemispherectomies) performed for the treatment of intractable childhood
555 epilepsy. *Acta Neuropathol*. 1992;83(3):246-259.
556 http://www.ncbi.nlm.nih.gov/pubmed/1557956.

557 12. Nordborg C, Eriksson S, Rydenhag B, Uvebrant P, Malmgren K. Microdysgenesis in
558 surgical specimens from patients with epilepsy: occurrence and clinical correlations. *J*
559 *Neurol Neurosurg Psychiatry*. 1999;67(4):521-524.
560 http://www.ncbi.nlm.nih.gov/pubmed/10486403.

561 13. Lee KS, Schottler F, Collins JL, et al. A genetic animal model of human neocortical
562 heterotopia associated with seizures. *J Neurosci*. 1997;17(16):6236-6242.
563 doi:10.1523/jneurosci.17-16-06236.1997

564 14. Bai J, Ramos RL, Ackman JB, Thomas AM, Lee R V., LoTurco JJ. RNAi reveals
565 doublecortin is required for radial migration in rat neocortex. *Nat Neurosci*.
566 2003;6(12):1277-1283. doi:10.1038/nn1153

567 15. Rosen GD, Sherman GF, Richman JM, Stone L V., Galaburda AM. Induction of molecular
568 layer ectopias by puncture wounds in newborn rats and mice. *Dev Brain Res*.
569 1992;67(2):285-291. doi:10.1016/0165-3806(92)90229-P

570 16. Brunstrom JE, Gray-Swain MRR, Osborne PA, Pearlman AL. Neuronal Heterotopias in
571 the Developing Cerebral Cortex Produced by Neurotrophin-4. *Neuron*. 1997;18(3):505-
572 517. doi:10.1016/S0896-6273(00)81250-7

573 17. Riggs HE, McGrath JJ, Schwarz HP. Malformation of the adult brain (albino rat) resulting
574 from prenatal irradiation. *J Neuropathol Exp Neurol*. 1956;15(4):432-447.
575 doi:10.1097/00005072-195610000-00006

576 18. Sherman GF, Galaburda AM, Behan PO, Rosen GD. Neuroanatomical anomalies in
577 autoimmune mice. *Acta Neuropathol*. 1987;74(3):239-242. doi:10.1007/BF00688187

578 19. Amano S, Ihara N, Uemura S, et al. Development of a Novel Rat Mutant with
579 Spontaneous Limbic-Like Seizures. *Am J Pathol*. 1996;149(1):329–336.

580 20. Dvořàk K, Feit J, Juránková Z. Experimentally induced focal microgyria and status
581 verrucosus deformis in rats - Pathogenesis and interrelation histological and
582 autoradiographical study. *Acta Neuropathol*. 1978;44(2):121-129.
583 doi:10.1007/BF00691477

584 21. Ferrer I, Alcántara S, Catalá I, Zújar MJ. Experimentally induced laminar necrosis, status
585 verrucosus, focal cortical dysplasia reminiscent of microgyria, and porencephaly in the
586 rat. *Exp brain Res*. 1993;94(2):261-269. http://www.ncbi.nlm.nih.gov/pubmed/8359242.
587 Accessed July 14, 2017.

588 22. Lo Turco J, Manent JB, Sidiqi F. New and improved tools for in utero electroporation
589 studies of developing cerebral cortex. *Cereb Cortex*. 2009;19(Suppl. 1):i120-5.
590 doi:10.1093/cercor/bhp033

591 23. Saito T, Nakatsuji N. Efficient Gene Transfer into the Embryonic Mouse Brain Using in
592 Vivo Electroporation. *Dev Biol*. 2001;240(1):237-246. doi:10.1006/dbio.2001.0439

593 24. Tabata H, Nakajima K. Efficient in utero gene transfer system to the developing mouse
594 brain using electroporation: Visualization of neuronal migration in the developing cortex.
595 *Neuroscience*. 2001. doi:10.1016/S0306-4522(01)00016-1

596 25. Schain AJ, Hill RA, Grutzendler J. Label-free in vivo imaging of myelinated axons in
597 health and disease with spectral confocal reflectance microscopy. *Nat Med*.
598 2014;20(4):443-449. doi:10.1038/nm.3495

599 26. Hill RA, Li AM, Grutzendler J. Lifelong cortical myelin plasticity and age-related
600 degeneration in the live mammalian brain. *Nat Neurosci*. 2018;21(May):1-13.
601 doi:10.1038/s41593-018-0120-6

602 27. Hill RA, Grutzendler J. In vivo imaging of oligodendrocytes with sulforhodamine 101. *Nat*
603 *Methods*. 2014;11(11):1081-1082. doi:10.1038/nmeth.3140

604 28. Jacob H. Die feinere Oberflächengestaltung der Hirnwindungen, die Hirnwarzenbildung
605 und die Mikropolygyrie. *Zeitschrift für die gesamte Neurol und Psychiatr*. 1940;170:68-84.
606 doi:10.1007/bf02869355

607 29. Morel F, Wildi E. Dysgénésie nodulaire disséminée de l'écorce frontale. *Rev Neurol*
608 *(Paris)*. 1952;87(3):251-270.

609 30. Sherman GF, Stone JS, Press DM, Rosen GD, Galaburda AM. Abnormal architecture
610 and connections disclosed by neurofilament staining in the cerebral cortex of autoimmune
611 mice. *Brain Res*. 1990;529(1-2):202-207. doi:10.1016/0006-8993(90)90828-Y

612 31. Ramos RL, Smith PT, DeCola C, Tam D, Corzo O, Brumberg JC. Cytoarchitecture and
613 Transcriptional Profiles of Neocortical Malformations in Inbred Mice. *Cereb Cortex*.
614 2008;18(11):2614-2628. doi:10.1093/cercor/bhn019

615 32. Sherman GF, Galaburda AM, Geschwind N. Cortical anomalies in brains of New Zealand

616 mice: a neuropathologic model of dyslexia? *Proc Natl Acad Sci U S A*. 1985;82(23):8072-
617 8074. doi:10.1073/pnas.82.23.8072

618 33. Ramos RL, Siu NY, Brunken WJ, et al. Cellular and axonal constituents of neocortical
619 molecular layer heterotopia. *Dev Neurosci*. 2014;36(6):477-489. doi:10.1159/000365100

620 34. Er JC, Leong C, Teoh CL, et al. NeuO: a Fluorescent Chemical Probe for Live Neuron
621 Labeling. *Angew Chemie Int Ed*. 2015;54(8):2442-2446. doi:10.1002/anie.201408614

622 35. Humphreys P, Kaufmann WE, Galaburda AM. Developmental dyslexia in women:
623 neuropathological findings in three patients. *Ann Neurol*. 1990;28(6):727-738.
624 doi:10.1002/ana.410280602

625 36. Galaburda AM, Sherman GF, Rosen GD, Aboitiz F, Geschwind N. Developmental
626 dyslexia: Four consecutive patients with cortical anomalies. *Ann Neurol*. 1985;18(2):222-
627 233. doi:10.1002/ana.410180210

628 37. Molyneaux BJ, Arlotta P, Fame RM, MacDonald JL, MacQuarrie KL, Macklis JD. Novel
629 subtype-specific genes identify distinct subpopulations of callosal projection neurons. *J*
630 *Neurosci*. 2009;29(39):12343-12354. doi:10.1523/jneurosci.6108-08.2009

631 38. Molyneaux BJ, Goff LA, Brettler AC, et al. DeCoN: Genome-wide Analysis of In Vivo
632 Transcriptional Dynamics during Pyramidal Neuron Fate Selection in Neocortex. *Neuron*.
633 2015;85(2):275-288. doi:https://doi.org/10.1016/j.neuron.2014.12.024

634 39. Sorensen SA, Bernard A, Menon V, et al. Correlated Gene Expression and Target
635 Specificity Demonstrate Excitatory Projection Neuron Diversity. *Cereb Cortex*.
636 2015;25(2):433-449. doi:10.1093/cercor/bht243

637 40. Gabel LA, LoTurco JJ. Electrophysiological and morphological characterization of
638 neurons within neocortical ectopias. *J Neurophysiol*. 2001;85(2):495-505.

639 doi:10.1152/jn.2001.85.2.495

640 41. Gabel LA. Layer I neocortical ectopia: Cellular organization and local cortical circuitry.
641 *Brain Res*. 2011;1381:148-158. doi:10.1016/J.BRAINRES.2011.01.040

642 42. Angevine JB, Sidman RL. Autoradiographic Study of Cell Migration during Histogenesis
643 of Cerebral Cortex in the Mouse. *Nature*. 1961;192(4804):766-768.
644 doi:10.1038/192766b0

645 43. Raedler E, Raedler A. Autoradiographic study of early neurogenesis in rat neocortex.
646 *Anat Embryol (Berl)*. 1978;154(3):267-284. doi:10.1007/bf00345657

647 44. Hill RA, Damisah EC, Chen F, Kwan AC, Grutzendler J. Targeted two-photon chemical
648 apoptotic ablation of defined cell types in vivo. *Nat Commun*. 2017;8(May):1-15.
649 doi:10.1038/ncomms15837

650 45. Singh SC. Ectopic neurones in the hippocampus of the postnatal rat exposed to
651 methylazoxymethanol during foetal development. *Acta Neuropathol*. 1977;40(2):111-116.
652 doi:10.1007/bf00688698

653 46. Rosen GD, Bai J, Wang Y, et al. Disruption of Neuronal Migration by RNAi of Dyx1c1
654 Results in Neocortical and Hippocampal Malformations. *Cereb Cortex*. 2007;17(11):2562-
655 2572. doi:10.1093/cercor/bhl162

656 47. Bagnard D, Lohrum M, Uziel D, Püschel AW, Bolz J. Semaphorins act as attractive and
657 repulsive guidance signals during the development of cortical projections. *Development*.
658 1998;125(24):5043-5053. http://www.ncbi.nlm.nih.gov/pubmed/9811588.

659 48. Richards LJ, Koester SE, Tuttle R, O'Leary DD. Directed growth of early cortical axons is
660 influenced by a chemoattractant released from an intermediate target. *J Neurosci*.
661 1997;17(7):2445-2458. http://www.ncbi.nlm.nih.gov/pubmed/9065505.

662 49. Métin C, Deléglise D, Serafini T, Kennedy TE, Tessier-Lavigne M. A role for netrin-1 in
663 the guidance of cortical efferents. *Development*. 1997;124(24):5063-5074.
664 https://www.scopus.com/inward/record.uri?eid=2-s2.0-
665 0031441084&partnerID=40&md5=16c8fc81c15621923b5da3fd9e86e059. Accessed
666 September 23, 2019.

667 50. Polleux F, Giger RJ, Ginty DD, Kolodkin AL, Ghosh A. Patterning of cortical efferent
668 projections by semaphorin-neuropilin interactions. *Science (80-)*. 1998;282(5395):1904-
669 1906. doi:10.1126/science.282.5395.1904

670 51. Gao PP, Yue Y, Zhang JH, Cerretti DP, Levitt P, Zhou R. Regulation of thalamic neurite
671 outgrowth by the Eph ligand ephrin-A5: implications in the development of thalamocortical
672 projections. *Proc Natl Acad Sci U S A*. 1998;95(9):5329-5334.
673 doi:10.1073/pnas.95.9.5329

674 52. Baudet M-L, Zivraj KH, Abreu-Goodger C, et al. miR-124 acts through CoREST to control
675 onset of Sema3A sensitivity in navigating retinal growth cones. *Nat Neurosci*.
676 2012;15(1):29-38. doi:10.1038/nn.2979

677 53. Shewan D, Dwivedy A, Anderson R, Holt CE. Age-related changes underlie switch in
678 netrin-1 responsiveness as growth cones advance along visual pathway. *Nat Neurosci*.
679 2002;5(10):955-962. doi:10.1038/nn919

680 54. Skaliora I, Singer W, Betz H, Püschel AW. Differential patterns of semaphorin expression
681 in the developing rat brain. *Eur J Neurosci*. 1998;10(4):1215-1229. doi:10.1046/j.1460-
682 9568.1998.00128.x

683 55. Sturrock RR. Myelination of the mouse corpus callosum. *Neuropathol Appl Neurobiol*.
684 1980;6(6):415-420. doi:10.1111/j.1365-2990.1980.tb00219.x

685 56. Goebbels S, Wieser GL, Pieper A, et al. A neuronal PI(3,4,5)P3-dependent program of
686 oligodendrocyte precursor recruitment and myelination. *Nat Neurosci*. 20(1):10-15.
687 doi:10.1038/nn.4425

688 57. Tomassy GS, Berger DR, Chen H-HH, et al. Distinct Profiles of Myelin Distribution Along
689 Single Axons of Pyramidal Neurons in the Neocortex. *Science (80-)*.
690 2014;344(6181):319-324. doi:10.1126/science.1249766

691 58. Micheva KD, Wolman D, Mensh BD, et al. A large fraction of neocortical myelin
692 ensheathes axons of local inhibitory neurons. *Elife*. 2016;5. doi:10.7554/eLife.15784

693 59. Ishii K, Kubo KI, Endo T, et al. Neuronal heterotopias affect the activities of distant brain
694 areas and lead to behavioral deficits. *J Neurosci*. 2015. doi:10.1523/JNEUROSCI.3648-
695 14.2015

696 60. Roper SN, Gilmore RL, Houser CR. Experimentally induced disorders of neuronal
697 migration produce an increased propensity for electrographic seizures in rats. *Epilepsy*
698 *Res*. 1995;21(3):205-219. doi:10.1016/0920-1211(95)00027-8

699 61. Nieto M, Monuki ES, Tang H, et al. Expression of Cux-1 and Cux-2 in the subventricular
700 zone and upper layers II-IV of the cerebral cortex. *J Comp Neurol*. 2004;479(2):168-180.
701 doi:10.1002/cne.20322

702 62. Chmielowska J, Stewart MG, Bourne RC. gamma-Aminobutyric acid (GABA)
703 immunoreactivity in mouse and rat first somatosensory (SI) cortex: description and
704 comparison. *Brain Res*. 1988;439(1-2):155-168. doi:10.1016/0006-8993(88)91472-2

705 63. Meyer HS, Schwarz D, Wimmer VC, et al. Inhibitory interneurons in a cortical column
706 form hot zones of inhibition in layers 2 and 5A. *Proc Natl Acad Sci*. 2011;108(40):16807-
707 16812. doi:10.1073/pnas.1113648108

708 64. Gabel LA, LoTurco JJ. Layer I Ectopias and Increased Excitability in Murine Neocortex. *J*
709 *Neurophysiol*. 2002;87(5):2471-2479. doi:10.1152/jn.2002.87.5.2471

710 65. Manent JB, Wang Y, Chang Y, Paramasivam M, LoTurco JJ. Dcx reexpression reduces
711 subcortical band heterotopia and seizure threshold in an animal model of neuronal
712 migration disorder. *Nat Med*. 2009;15(1):84-90. doi:10.1038/nm.1897

713 66. Chevassus-Au-Louis N, Rafiki A, Jorquera I, Ben-Ari Y, Represa A. Neocortex in the
714 hippocampus: An anatomical and functional study of CA1 heterotopias after prenatal
715 treatment with methylazoxymethanol in rats. *J Comp Neurol*. 1998;394(4):520-536.
716 doi:10.1002/(SICI)1096-9861(19980518)394:4<520::AID-CNE9>3.0.CO;2-3

717 67. Jenner AR, Galaburda AM, Sherman GF. Connectivity of ectopic neurons in the
718 molecular layer of the somatosensory cortex in autoimmune mice. 2000;10(10):1005-
719 1013.

720 68. Chevassus-Au-Louis N, Congar P, Represa A, Ben-Ari Y, Gaïarsa JL. Neuronal migration
721 disorders: heterotopic neocortical neurons in CA1 provide a bridge between the
722 hippocampus and the neocortex. *Proc Natl Acad Sci U S A*. 1998;95(17):10263-10268.
723 doi:10.1073/PNAS.95.17.10263

724 69. Schottler F, Fabiato H, Leland JM, et al. Normotopic and heterotopic cortical
725 representations of mystacial vibrissae in rats with subcortical band heterotopia.
726 *Neuroscience*. 2001. doi:10.1016/S0306-4522(01)00395-5

727 70. Romero DM, Bahi-Buisson N, Francis F. Genetics and mechanisms leading to human
728 cortical malformations. *Semin Cell Dev Biol*. 2018;76:33-75.
729 doi:10.1016/J.SEMCDB.2017.09.031

730 71. Saito T. In vivo electroporation in the embryonic mouse central nervous system. *Nat*

Protoc. 2006;1(3):1552-1558. doi:10.1038/nprot.2006.276

72. Kim J-Y, Ash RT, Ceballos-Diaz C, et al. Viral transduction of the neonatal brain delivers controllable genetic mosaicism for visualising and manipulating neuronal circuits in vivo. *Eur J Neurosci*. 2013;37(8):1203-1220. doi:10.1111/ejn.12126

73. Phifer CB, Terry LM. Use of hypothermia for general anesthesia in preweanling rodents. *Physiol Behav*. 1986;38(6):887-890.

74. Patel TP, Man K, Firestein BL, Meaney DF. Automated quantification of neuronal networks and single-cell calcium dynamics using calcium imaging. *J Neurosci Methods*. 2015;243:26-38. doi:10.1016/j.jneumeth.2015.01.020

75. Li X, Ouyang G, Usami A, Ikegaya Y, Sik A. Scale-Free Topology of the CA3 Hippocampal Network: A Novel Method to Analyze Functional Neuronal Assemblies. *Biophys J*. 2010;98(9):1733-1741. doi:10.1016/J.BPJ.2010.01.013

76. Li X, Cui D, Jiruska P, Fox JE, Yao X, Jefferys JGR. Synchronization Measurement of Multiple Neuronal Populations. *J Neurophysiol*. 2007;98(6):3341-3348. doi:10.1152/jn.00977.2007

ACKNOWLEDGEMENTS

We thank F. Chen for his guidance *in utero* electroporation techniques. This study was funded by grants from the U.S. National Institutes of Health (R01NS089734, R21NS088411 and R21NS087511 to J.G.; R00NS099469 and P20GM113132 to R.A.H.; T32NS007224 and T32GM007205 to A.M.L.), Donors Cure Foundation (New Vision Award to R.A.H.), and National Multiple Sclerosis Society (#RR-1602-07686 to J.G.).

AUTHOR CONTRIBUTIONS

A.M.L. and J.G. conceived the initial project. A.M.L., R.A.H, and J.G. designed the experiments. A.M.L. performed all experiments, analyzed the data, and prepared the figures. A.M.L., R.A.H. and J.G. wrote the manuscript.

COMPETING INTERESTS

The authors declare no competing interests.

MATERIALS & CORRESPONDENCE

Correspondence and requests for materials should be addressed to J.G. (email: jaime.grutzendler@yale.edu) and R.A.H. (email: robert.hill@dartmouth.edu).

768 **Fig. 1. Targeted induction and high-resolution imaging of layer I heterotopia in the live**
769 **mouse. a**, Diagram showing a single neocortical heterotopion induced at the needle tract
770 during *in utero* electroporation (IUE) at embryonic day (E15). The site is relocated postnatally for
771 detailed investigation of the resulting layer I heterotopion by intravital imaging. **b**, Quantification
772 showing significantly increased neuron density (n = 6 mice) within heterotopia compared to
773 ipsilateral neighboring layer I control regions (Wilcoxon non-parametric, matched-pairs signed
774 rank test *P < 0.05). Each point represents the heterotopion or control region from one animal.
775 Horizontal lines and error bars denote mean and s.e.m, respectively. Descriptive statistics are
776 indicated in Supplementary File 1. **c**, *In vivo* fluorescence images of a representative layer
777 I heterotopion (right) and neighboring ipsilateral, non-injected control region in a P30 mouse (left).
778 Notice the tightly packed cluster of fluorescently labelled neuronal cell bodies (NeuO; green).
779 Neurons within the heterotopion can also be readily labeled during the electroporation procedure
780 and visualized *in vivo* (tdTomato; red). In contrast, neurons in more sparsely populated control
781 layer I regions never demonstrate IUE-mediated labelling (left column). HTP, heterotopia. Scale
782 bars, 50 μm (**c**).

783 **Fig. 2. Heterotopia contain an abundance of hypermyelinated axons. a**, *In vivo* combined
784 fluorescence and label-free SCoRe myelin images of a representative induced heterotopion (right;
785 same as in Figure 1c) and neighboring ipsilateral, non-injected control region (left) in a P30
786 mouse. The tightly packed heterotopic neuronal cell bodies (NeuO) are surrounded by a
787 circumscribed abundance of aberrantly projecting, myelinated axon segments (SCoRe). **b**,**c** Low
788 magnification (**b**) and high magnification (**c**) immunostainings of an induced heterotopion and its
789 corresponding contralateral control region taken from a P30 mouse, showing increased
790 oligodendrocyte CNPase expression associated with the heterotopion, as defined by the
791 ectopically positioned $NeuN^+$ neuronal cell bodies in layer I (**b**, white arrowheads). Notice the
792 more horizontal orientation of myelin segments located closer to the pial surface of the
793 heterotopion (**c**, blue arrowhead). Deeper myelin segments, in contrast, are organized in a more
794 radial fashion (**c**, blue arrow) and fasciculate into densely myelinated fiber bundles that project
795 through lower cortical layers (**b**, white arrow). **d**, Quantifications of SCoRe *in vivo* (n = 8 mice;
796 top) and CNPase in fixed tissue (n = 6 mice; middle and bottom), showing increased myelination
797 and oligodendrocyte cell body densities in induced layer I heterotopia compared to non-injected
798 contralateral control regions. Each point represents the layer I heterotopion or control region from
799 one animal. Horizontal lines and error bars denote mean and s.e.m, respectively (Wilcoxon
800 matched-pairs signed rank non-parametric test; $^*P < 0.05$, $^{**}P < 0.01$). HTP, Heterotopia.
801 Descriptive statistics are given in Supplementary File 1. Scale bars, 50 μm (**a**), 200 μm in (**b**), and
802 50 μm (**c**).

803 **Fig. 3. Myelinated and unmyelinated axons follow aberrantly looping and concentric paths.**
804 **a-d**, Intravital imaging of a nest-like heterotopion at P30 in (**a**) using SCoRe and confocal
805 fluorescence microscopy showing **b**, labelled neuronal cell bodies (tdTomato; green) dispersed
806 throughout the aberrantly oriented myelinated fibers (SCoRe; magenta) and **c**, winding axonal
807 projections that occasionally fasciculate into bundles at the edges of the heterotopion. **d**,
808 Myelinated (arrowheads) and unmyelinated axon segments (arrows) are observed within the
809 heterotopion. **e-g**, Low magnification (**e**) and high magnification (**f**, **g**) immunostainings of an
810 embryonically-induced heterotopion, confirming the presence of both myelinated (**g**, arrowhead)
811 and unmyelinated (**f**, arrow) axon segments (**f** and **g** show high magnification images of areas
812 indicated by arrow and arrowhead in **e**, respectively). NF-H, neurofilament heavy chain. Images
813 are representative of experiments performed in at least six animals. Scale bars, 100 μm (**a**), 15
814 μm (**b**-**d**), 100 μm (**e**), and 25 μm (**f**, **g**).

815 **Fig. 4. Heterotopia can be induced at various embryonic stages of corticogenesis. a**, *In vivo*
816 NeuO dye neuron staining (green) and SCoRe myelin imaging (magenta) of P30 mouse cortices
817 that were previously electroporated at E14 (left column), E15 (middle column), and E17 (right
818 column), all showing similar aberrantly projecting axons and hypermyelination encircling ectopic
819 neuron clusters. Images are representative of observations made in at least three animals per
820 IUE-injected age group. Scale bars, 100 μm.

821 **Fig. 5. Postnatally-induced heterotopia do not develop aberrant axons or myelination. a**,
822 Confocal images of an immunolabelled coronal section from P30 mouse cortex, showing no
823 changes in myelination (CNPase) or axonal pathfinding (NF-H) associated with a P0-induced
824 heterotopion (NeuN; arrowheads), compared to its contralateral control region (left). **b**, In contrast,
825 neuronal heterotopia induced *in utero* at E15 (NeuN; arrowheads) show dramatic changes in local
826 layer I myelin (CNPase) expression and patterning. **c**, Quantifications of CNPase expression,
827 showing no significant differences in the myelin or oligodendrocyte cell body densities (n = 6
828 animals) between postnatally-induced heterotopia and control regions. Each point represents the
829 P0-induced layer I heterotopion or control region from one animal, with horizontal lines and error
830 bars denoting mean and s.e.m, respectively. Wilcoxon matched-pairs signed rank non-parametric
831 test was used to determine significance; NS, no significance. NF-H, neurofilament heavy chain.
832 Descriptive statistics are given in Supplementary File 1. Scale bars, 100 μm (**a**, **b**).

833 **Fig. 6. Astrocytes and microglia retain a normal density despite aberrant axonal and myelin**
834 **distribution. a-b**, Low magnification (**a**) and high magnification (**b**) images of Aldh1l1-positive
835 astrocytes in P30 mouse cortex, showing similar cell densities in layer I heterotopia (right images,
836 arrowheads) compared to corresponding contralateral control regions (left images). **c**,
837 Quantifications using P30 mouse forebrain tissue showing no significant difference in astrocyte
838 cell density (Wilcoxon non-parametric matched-pairs, signed rank test, *n* = 6 animals; ns, no
839 significance). **d-e** Low magnification (**d**) and high magnification (**e**) images of Iba1-
840 immunolabelled P30 mouse forebrain, showing no difference in microglia cell densities between
841 heterotopia (right images, arrowheads) and contralateral control regions (left images). **f**,
842 Quantifications using P30 mouse forebrain tissue demonstrating no significant difference in
843 microglia cell density between layer I heterotopia and corresponding contralateral control regions
844 (Wilcoxon matched-pairs, signed rank non-parametric test, *n* = 6 animals; ns, no significance).
845 For graphs in (**c**) and (**f**), each point represents an embryonically-induced layer I heterotopion or
846 control region from one animal, with horizontal lines and accompanying error bars denoting mean
847 and s.e.m., respectively. Descriptive statistics are given in Supplementary File 1. HTP,
848 heterotopia. Scale bars, 100 μm (**a**), 20 μm (**b**), 100 μm (**d**), and 20 μm (**e**).

849 **Fig. 7. Heterotopia contain a mixed population of excitatory and inhibitory neurons. a**,
850 Approach for quantifying layer-specific neuronal marker expression (symbolized by blue and
851 green dots) in layer I heterotopia and across corresponding contralateral control cortices in P30
852 mice. Contralateral control cortices are subdivided into 11 equally-sized bins that together span
853 the entire thickness of the cortex. **b**-**c** Both Cux1$^+$ (**b**, cyan) and Tle4$^+$ (**c**, green) neuronal cell
854 bodies occur within layer I heterotopia (right images, arrowheads). In contralateral control regions
855 (left images), Cux1 is concentrated in more superficial cortical areas corresponding to layers II/III,
856 whereas deeper areas corresponding to layers V/VI encapsulate the majority of Tle4 labelling.
857 Quantifications (far right) show the percentages of NeuN$^+$ cell bodies that also express Cux1 (top)
858 or Tle4 (bottom) within heterotopia and across corresponding contralateral control bins. Each dot
859 corresponds to the layer I heterotopion or control bin of a single animal, with all dots of the same
860 color belonging to the same animal (n = 4 animals for Cux1; n = 5 animals for Tle4). The black
861 line denotes the mean. WM, white matter. **d**,**e** Low (**d**) and high (**e**) magnification z-projections of
862 GAD-67-immunostained P30 mouse forebrain, showing the presence of GAD-67-labelled cells
863 and puncta in both layer I heterotopia (right images, arrowheads) and corresponding contralateral
864 control regions (left images). **f**, Quantifications from P30 mouse tissue showing no significant
865 difference in GAD-67$^+$ neuronal cell density between layer I heterotopia and contralateral control
866 regions (Wilcoxon matched-pairs, signed rank non-parametric test, n = 6 animals; ns, no
867 significance). Each point represents the layer I heterotopion or contralateral control region from
868 one animal, with horizontal lines and accompanying error bars denoting mean and s.e.m.,
869 respectively. HTP, heterotopia. Descriptive statistics are given in Supplementary File 1. Scale
870 bars 200 μm (**b**, **c**), 100 μm (**d**), and 10 μm (**e**).

871 **Fig. 8. Heterotopic neurons display calcium dynamics similar to adjacent layer II/III**
872 **neurons and respond to sensorimotor input. a-c** *In vivo* time lapse imaging of layer I
873 heterotopic neurons expressing the calcium sensor GCaMP6f in an awake, head-fixed mouse.
874 Dotted lines in (**a**) indicate an analyzed heterotopic region that is displayed in (**b**). **c**, Example
875 traces of spontaneous neuronal calcium transients from layer I heterotopic (right) and ipsilateral
876 layer II/III non-heterotopic (left) regions displayed in (**b**). **d**, Quantifications showing no significant
877 difference in calcium spike event frequency (Hz), variance (s.d.) or global synchronization index
878 between layer I heterotopia and adjacent layer II/III non-heterotopic regions. Each dot
879 corresponds to the average value for each measure in a layer I heterotopion or non-heterotopic
880 layer II/III region from a single animal. Data represent 493 layer I heterotopic neurons and 594
881 layer II/III neurons from n = 7 mice. Wilcoxon matched-pairs, signed rank non-parametric test was
882 used for all three quantifications; ns, no significance; HTP, heterotopia. Descriptive statistics are
883 given in Supplementary File 1. **e**, *In vivo* z-projection of the same GCaMP6f-transfected
884 heterotopion displayed in (**a**), captured at a different depth, showing neurons that were imaged
885 during brief applications of whisker stimulation. **f**, Baseline calcium dynamics (left column) and
886 calcium fluctuations (middle and right columns) of individual heterotopic neurons in response to
887 stimuli (denoted by solid blue line in two trials) obtained from the awake, head-fixed mouse
888 imaged in (**e**). Experimental observations in (**e**, **f**) were replicated in three mice. All data and
889 images from (**a-f**) were obtained from P50-60 mice with heterotopia induced at E15, and virally
890 transfected with AAV-GCaMP6f at P21-P30. Some neuronal cell body and axonal labelling by
891 pCAG-TdTomato (red) is the result of E15 IUE-mediated transfection. Scale bars, 50 μm (**a**), 25
892 μm (**b**), and 50 μm (**e**).

893 **Figure 3–figure supplement 1. Myelinated axons project aberrantly around heterotopic**
894 **cells. a**, High resolution immunostaining showing the winding trajectories followed by CNPase^{+}
895 fibers (bottom, blue arrow) within a layer I heterotopion (NeuN; white arrowheads) in a P30 mouse
896 coronal section. The aberrantly-projecting myelinated fiber bundles are absent from immediately
897 adjacent non-heterotopic cortex and corresponding contralateral control regions (top row).
898 Images are representative of experiments performed in at least six animals. Scale bars, 100 μm.

899 **Figure 2–figure supplement 1. Disrupted myelin patterning and axonal pathfinding occurs**
900 **in deeper cortical layers. a,** Myelinated fibers (MBP, cyan) accumulate in thick radially oriented
901 cords (white arrow) beneath a layer I heterotopion (NeuN; arrowheads) in an immunostained P30
902 mouse forebrain coronal section. **b-c,** Confocal images of a different coronal section from the
903 same heterotopion in (**a**), revealing similar aberrant myelin and axon accumulations as identified
904 by oligodendrocyte CNPase (green) and axonal NF-H (red) immunostaining, respectively**.** A
905 higher magnification view of the densely packed myelinated axons fasciculating underneath
906 the heterotopion (**b**, blue arrow) is shown in (**c**). Images in (**b**) and (**c**) are of same section shown
907 in Figure 3e**.** Images are representative of fixed tissue experiments performed in at least three
908 mice. Scale bars, 200 μm (**a**, **b**), and 20 μm (**c**).

909 **Figure 7–figure supplement 1. Heterotopic neurons express both deep and superficial**
910 **cortical layer markers. a-b**, Additional fixed tissue images captured from the heterotopia
911 displayed in Figures 7b and c, confirming the presence of Cux1$^+$ (**a**, cyan) and Tle4$^+$ (**b**, green)
912 neuronal cell bodies within the representative heterotopia (bottom images, arrowheads). In
913 corresponding contralateral control regions (top images), Cux1 (left) largely concentrates in
914 superficial cortical layers whereas Tle4 (right) tends to localize toward deeper cortical layers. **c-**
915 **d**, Quantifications showing the densities of Cux1$^+$ (**c**, *n* = 4 animals), Tle4$^+$ (**d**, *n* = 5 animals), and
916 NeuN$^+$ (**c** and **d**, right) cells in heterotopia and across corresponding contralateral control regions
917 of P30 mice. Each dot corresponds to the layer I heterotopion or control bin of a single animal,
918 with all dots of the same color belonging to the same animal. The black line denotes the mean.
919 Images are representative of experiments performed in at least four animals. WM, white matter;
920 HTP, heterotopia. Scale bars, 200 μm.

921 **Figure 7–figure supplement 2. Birth-dating of heterotopic neurons. a**, Diagram of the pulse
922 labelling strategy for birthdating heterotopic cortical neurons. Dividing cells are labelled by a single
923 EdU injection at E11.5, with heterotopia induced at E15. Mice are sacrificed at P30 for analysis.
924 **b**, Low magnification images showing the EdU^+ neurons incorporated in a layer I heterotopion
925 (right, arrowheads) of a P30 mouse. In corresponding contralateral control cortex (left column),
926 EdU expression is predominantly concentrated in deeper cortical layers. **c**, Quantifications
927 showing the percentages of $NeuN^+$ cells that also express EdU (top), EdU^+NeuN^+ cell body
928 densities (middle), and $NeuN^+$ cell body densities (bottom) in layer I heterotopia and across
929 corresponding contralateral control cortices of P30 mice. Each dot corresponds to the layer I
930 heterotopion or control bin of a single animal, with all dots of the same color belonging to the
931 same animal (*n* = 4 animals total). Images are representative of the observations made in each
932 mouse brain. The black line denotes the mean. WM, white matter; HTP, heterotopia. Scale bars,
933 200 μm.

934 **Video 1. *In vivo* imaging of a layer I heterotopion and adjacent control area.** Confocal z-
935 stacks of a heterotopion (right) and ipsilateral non-injected layer I control region (left) captured
936 from a living P30 mouse using label-free SCoRe (magenta) and fluorescence microscopy,
937 showing the aberrantly projecting myelinated axons and ectopic neurons located inside a layer I
938 heterotopion induced at E15. Neuronal cell bodies and cerebral blood vessels are visualized using
939 fluorescent neuronal dye NeuO (green) and Evans Blue (white), respectively. The density of the
940 horizontally crisscrossing, aberrantly projecting fibers diminishes with increasing cortical depth
941 (indicated at bottom left).

942 **Video 2. Layer I heterotopia and adjacent layer II/III regions display highly variable**
943 **spontaneous neuronal calcium transients.** Representative *in vivo* two-photon time-lapse
944 recordings of GCaMP6f-labelled neurons (green) within a layer I heterotopion (right) and an
945 adjacent layer II/III cortical region (left) in an awake, head-fixed P55 mouse. Diverse patterns of
946 spontaneous calcium transients are observed in neuronal cell bodies throughout both imaged
947 regions. Note the absence of obvious epileptiform activity. Images were acquired at 2 Hz from an
948 E15-induced layer I heterotopion. Some neuronal cell body and axonal labelling by pCAG-
949 TdTomato (red) is the result of E15 IUE-mediated transfection.

950 **Video 3. Heterotopic neurons respond to sensory stimuli.** Two *in vivo* confocal time-lapse
951 recording examples of GCaMP6f-labelled neurons within a layer I heterotopion before, during,
952 and after the application of a brief whisker stimulus, administered one minute into each imaging
953 session. The timing of the stimulus and accompanying movements are indicated by the white
954 circle (positioned at the top left of the embedded video). Neuronal calcium changes are observed
955 upon the application of each stimulus, indicating the responsiveness of the heterotopic neurons
956 to sensorimotor input. Both recordings were obtained from P55 awake, head-fixed mice with layer
957 I heterotopia that were induced at E15 and virally transfected using AAV-GCaMP6f at P21-P30.

958 **Supplementary Table 1.** Details for all statistical analyses, including sample sizes and p-values.

Figure 1

a

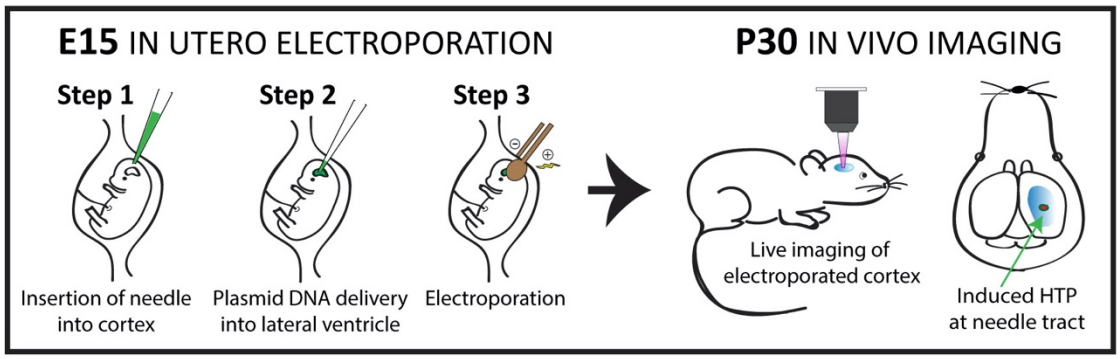
E15 IN UTERO ELECTROPORATION
P30 IN VIVO IMAGING
Step 1
Step 2
Step 3
Insertion of needle into cortex
Plasmid DNA delivery into lateral ventricle
Electroporation
Live imaging of electroporated cortex
Induced HTP at needle tract

b

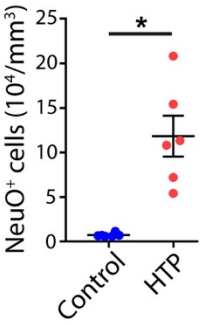
NeuO+ cells (10^4/mm^3)
25
20
15
10
5
0
*
Control
HTP

c

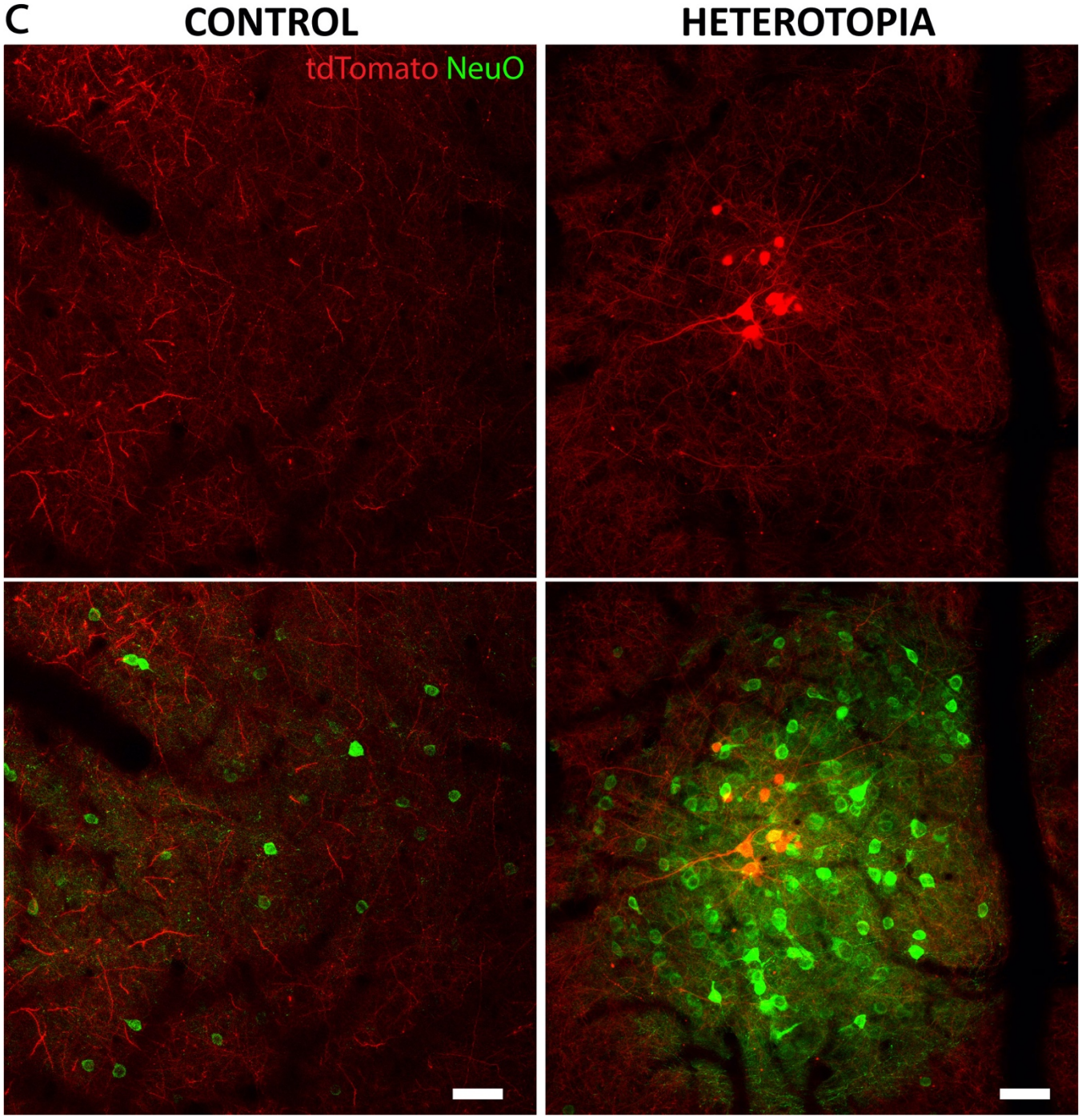
CONTROL
HETEROTOPIA
tdTomato NeuO

Figure 2

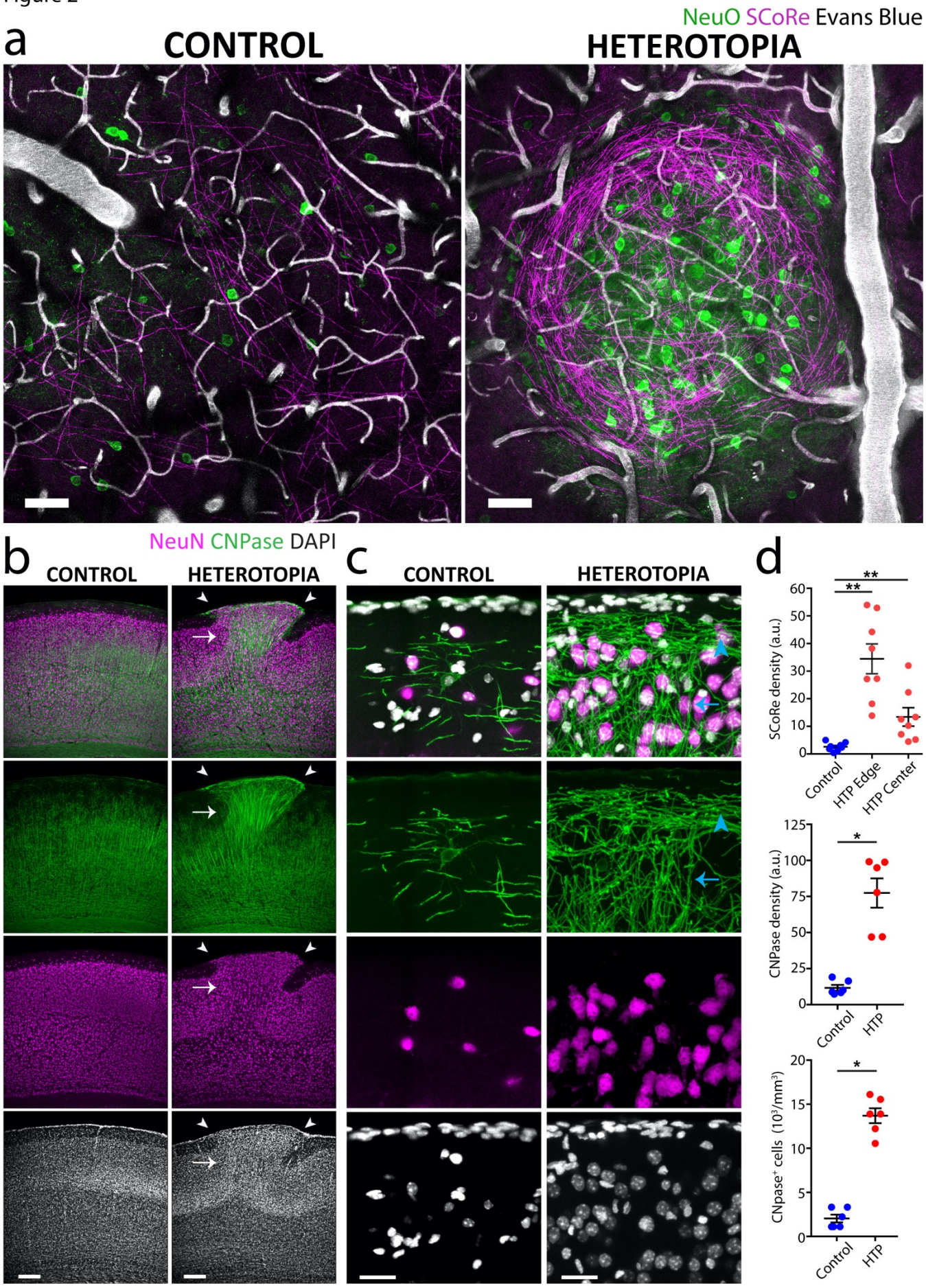
NeuO SCoRe Evans Blue
a
CONTROL
HETEROTOPIA
NeuN CNPase DAPI
b
CONTROL
HETEROTOPIA
c
CONTROL
HETEROTOPIA
d
SCoRe density (a.u.)
Control
HTP Edge
HTP Center
CNPase density (a.u.)
Control
HTP
CNpase+ cells (10³/mm³)
Control
HTP

Figure 2 - figure supplement 1

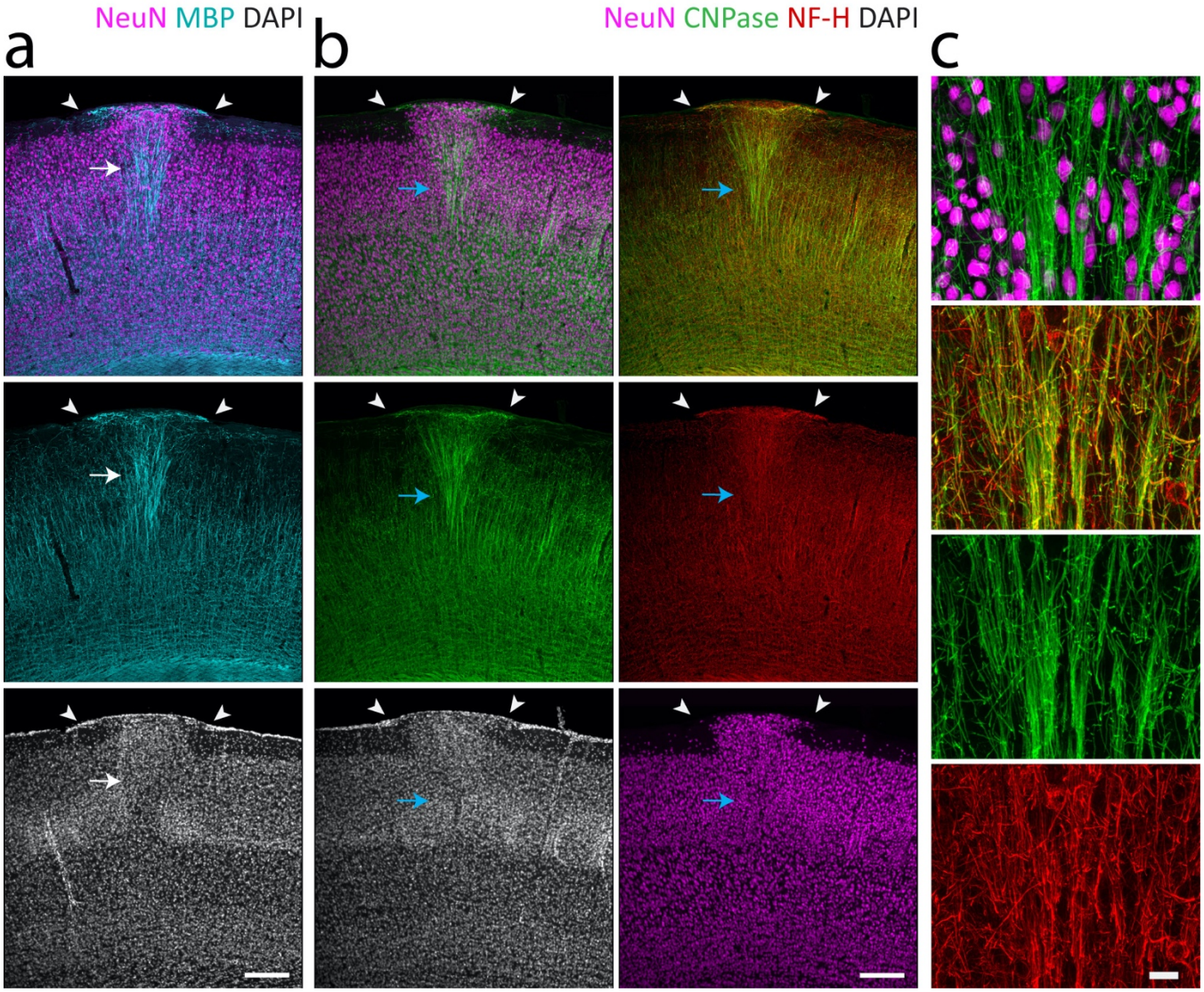

Figure 3

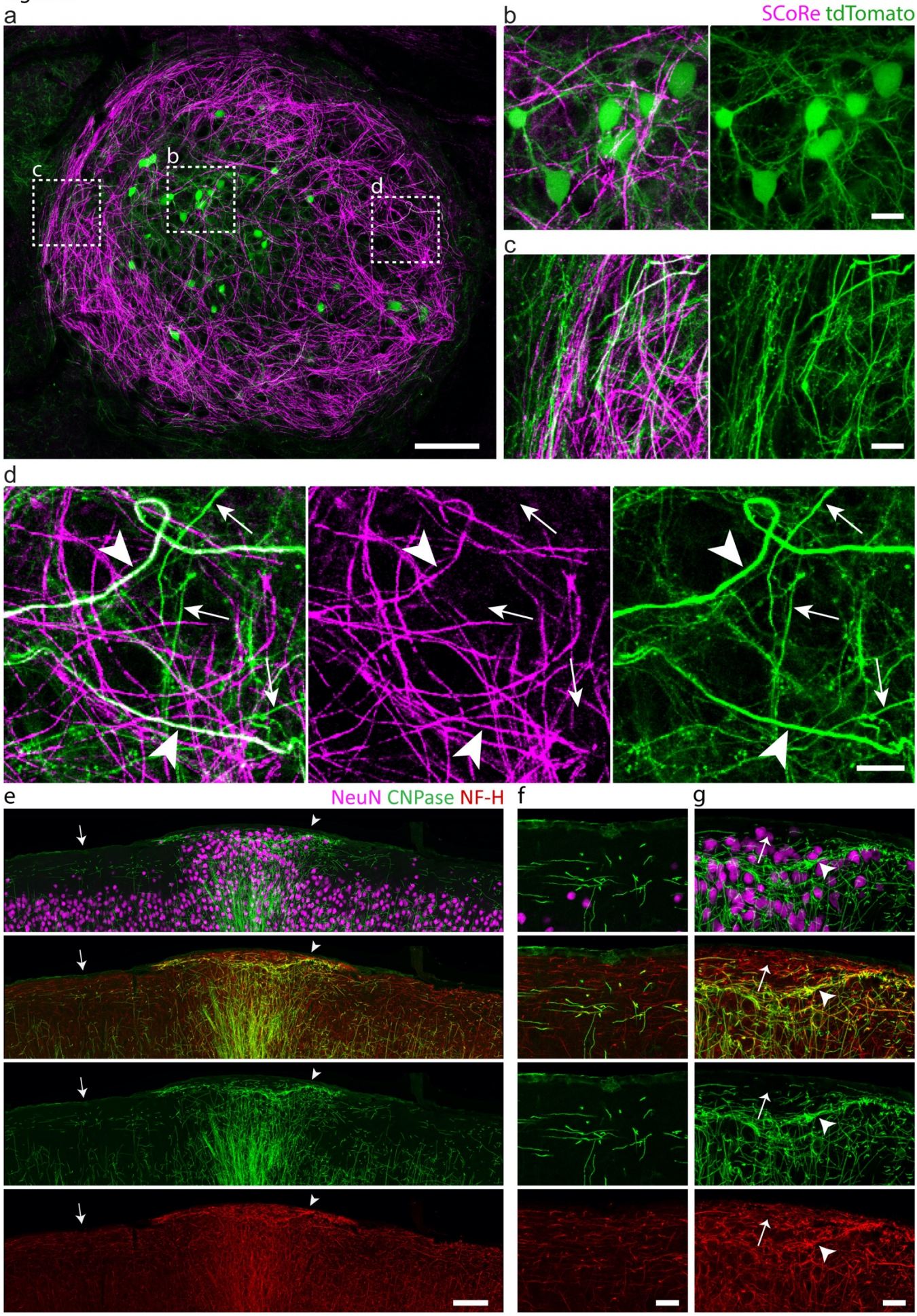

Figure 3 - figure supplement 1

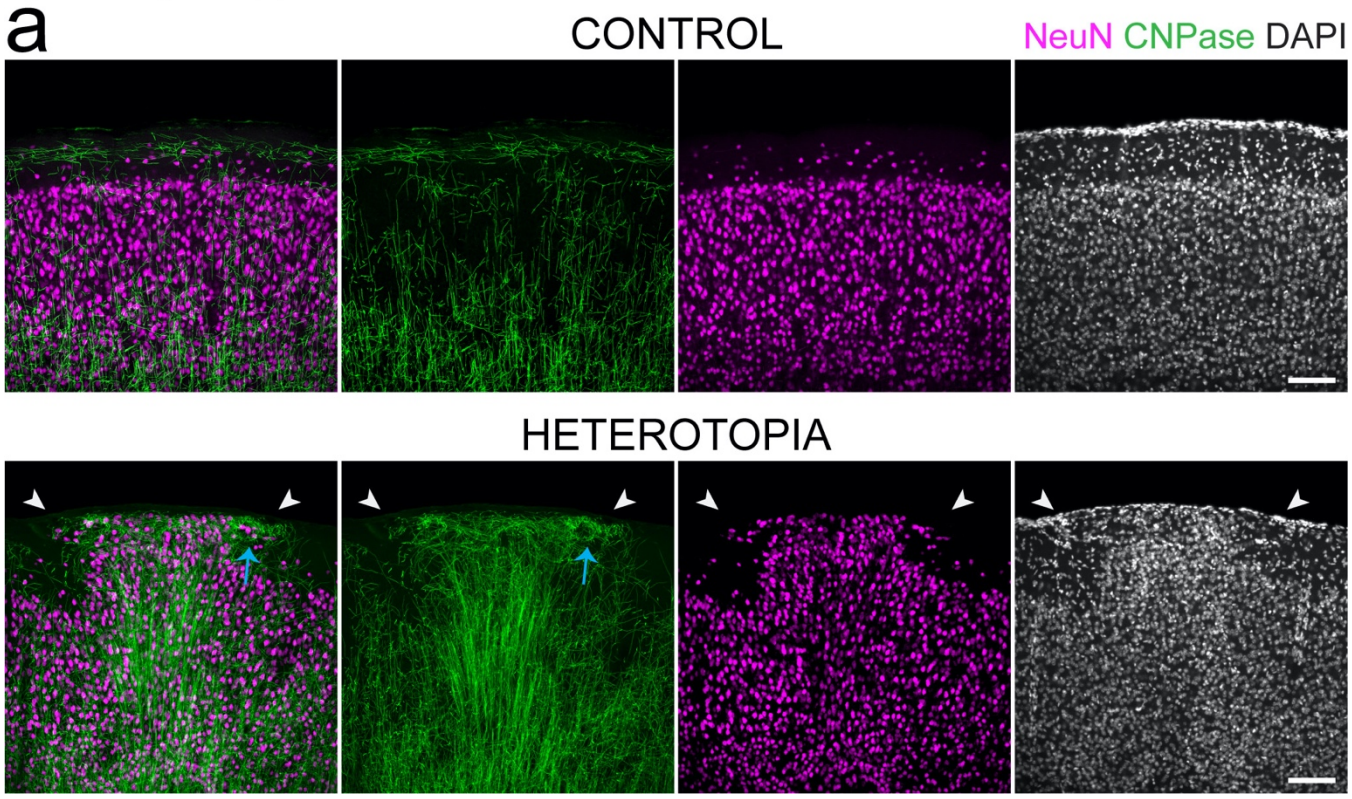

Figure 4

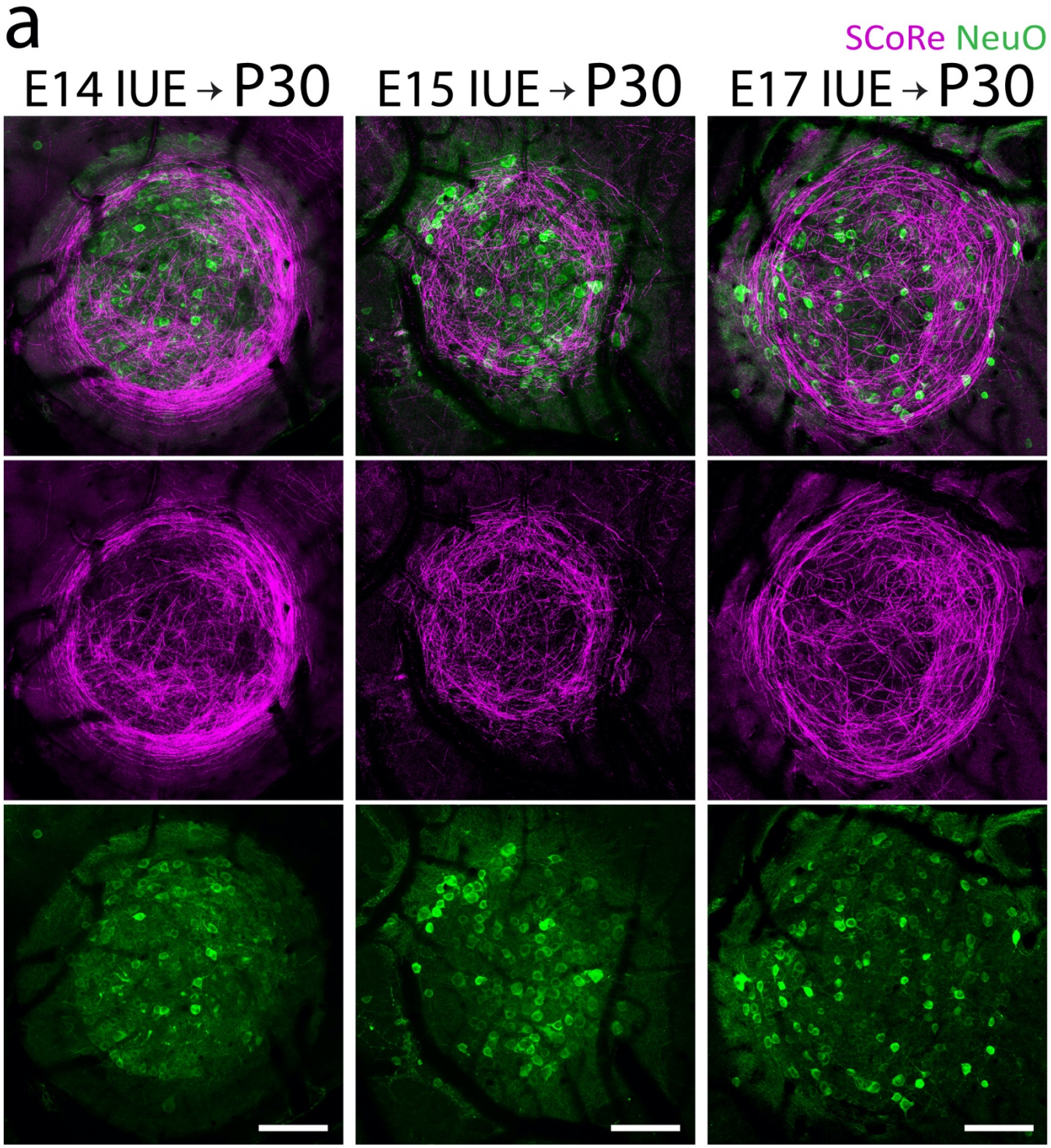

Figure 5

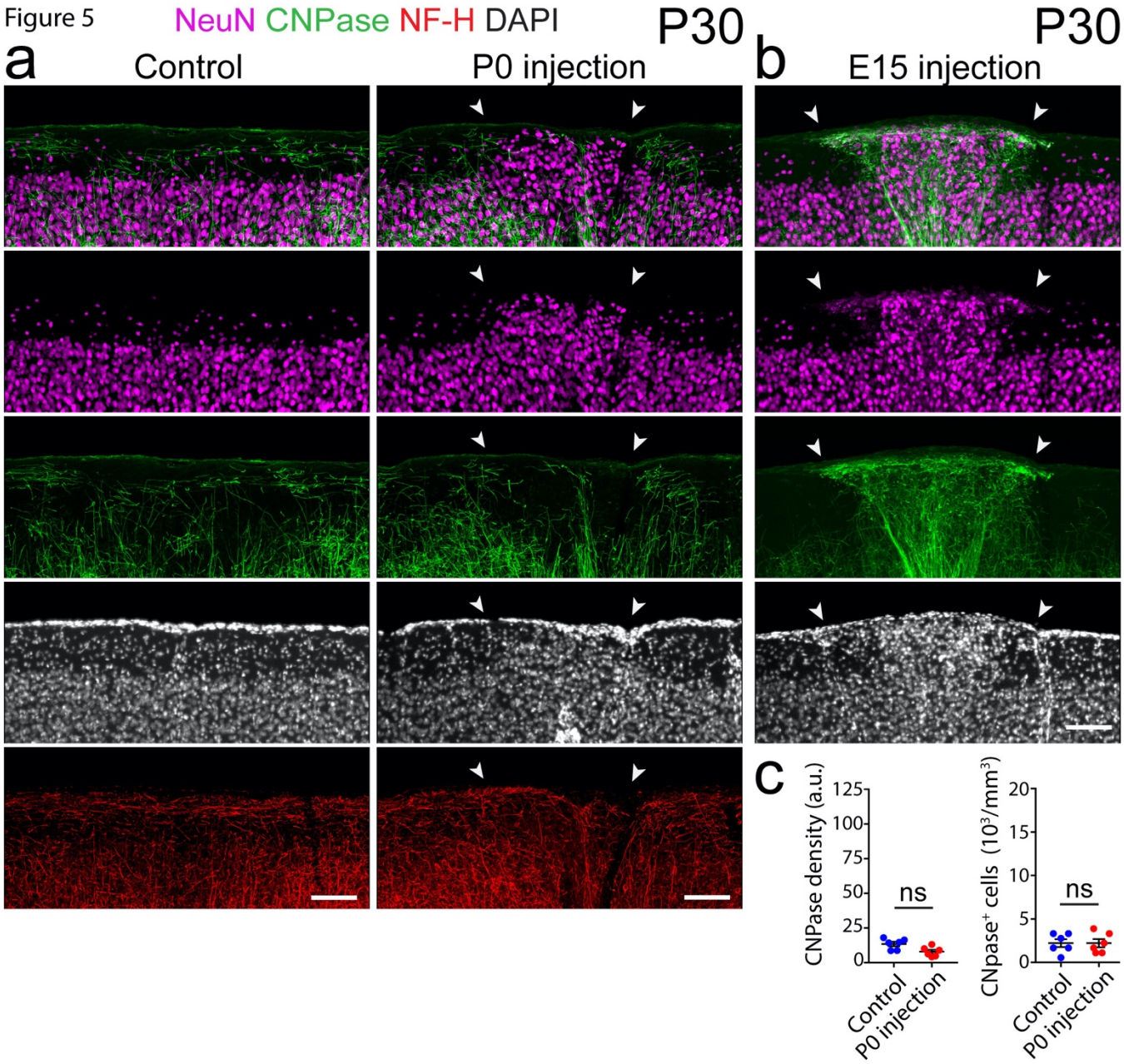
NeuN CNPase NF-H DAPI
P30
P30
a
Control
P0 injection
b
E15 injection
c
CNPase density (a.u.)
125
100
75
50
25
0
ns
Control
P0 injection
CNpase+ cells (10³/mm³)
20
15
10
5
0
ns
Control
P0 injection

Figure 6

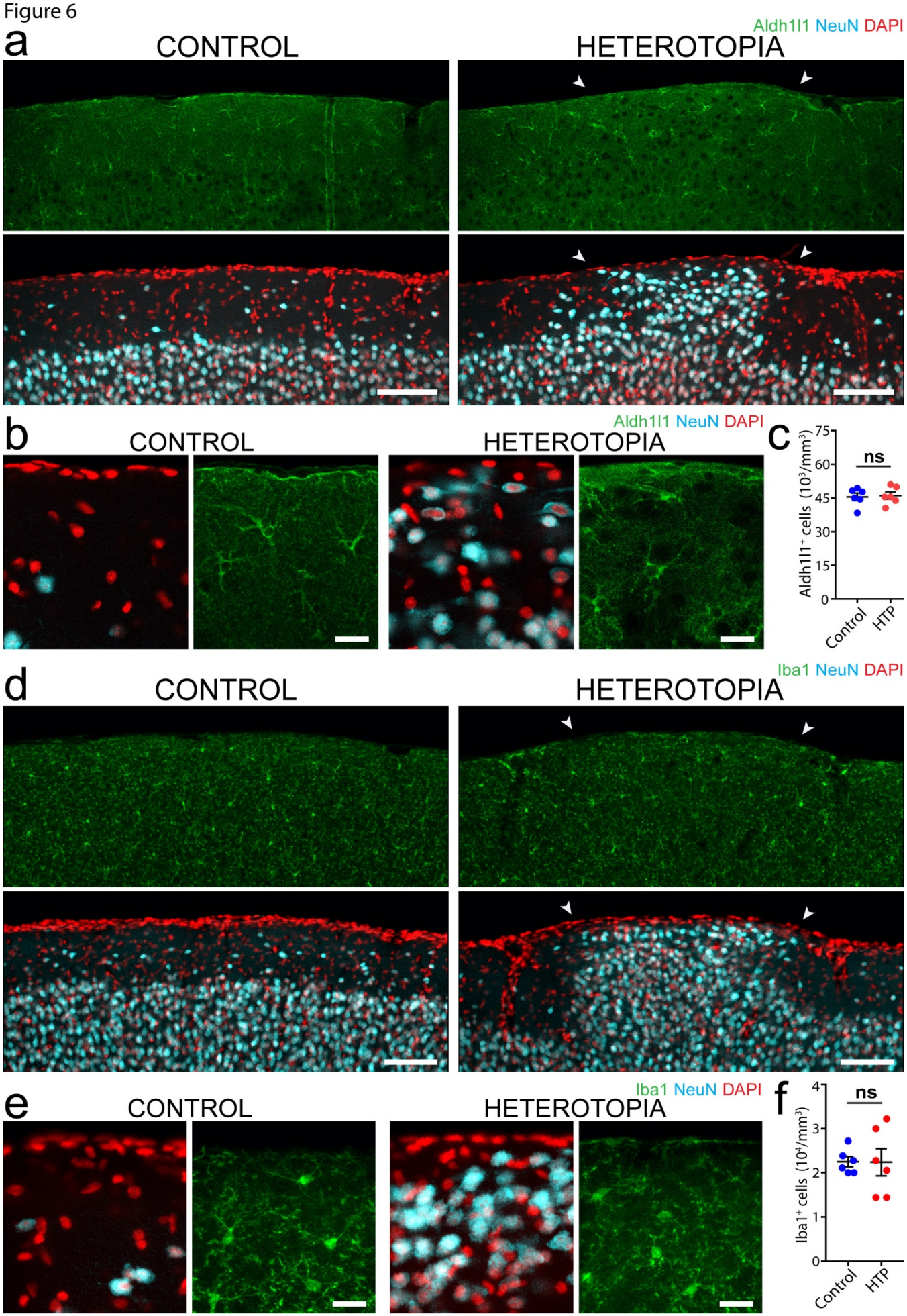
a
CONTROL
HETEROTOPIA
Aldh1l1 NeuN DAPI
b
CONTROL
HETEROTOPIA
Aldh1l1 NeuN DAPI
c
ns
Aldh1l1+ cells (10³/mm³)
75
60
45
30
15
0
Control
HTP
d
CONTROL
HETEROTOPIA
Iba1 NeuN DAPI
e
CONTROL
HETEROTOPIA
Iba1 NeuN DAPI
f
ns
Iba1+ cells (10⁴/mm³)
4
3
2
1
0
Control
HTP

Figure 7

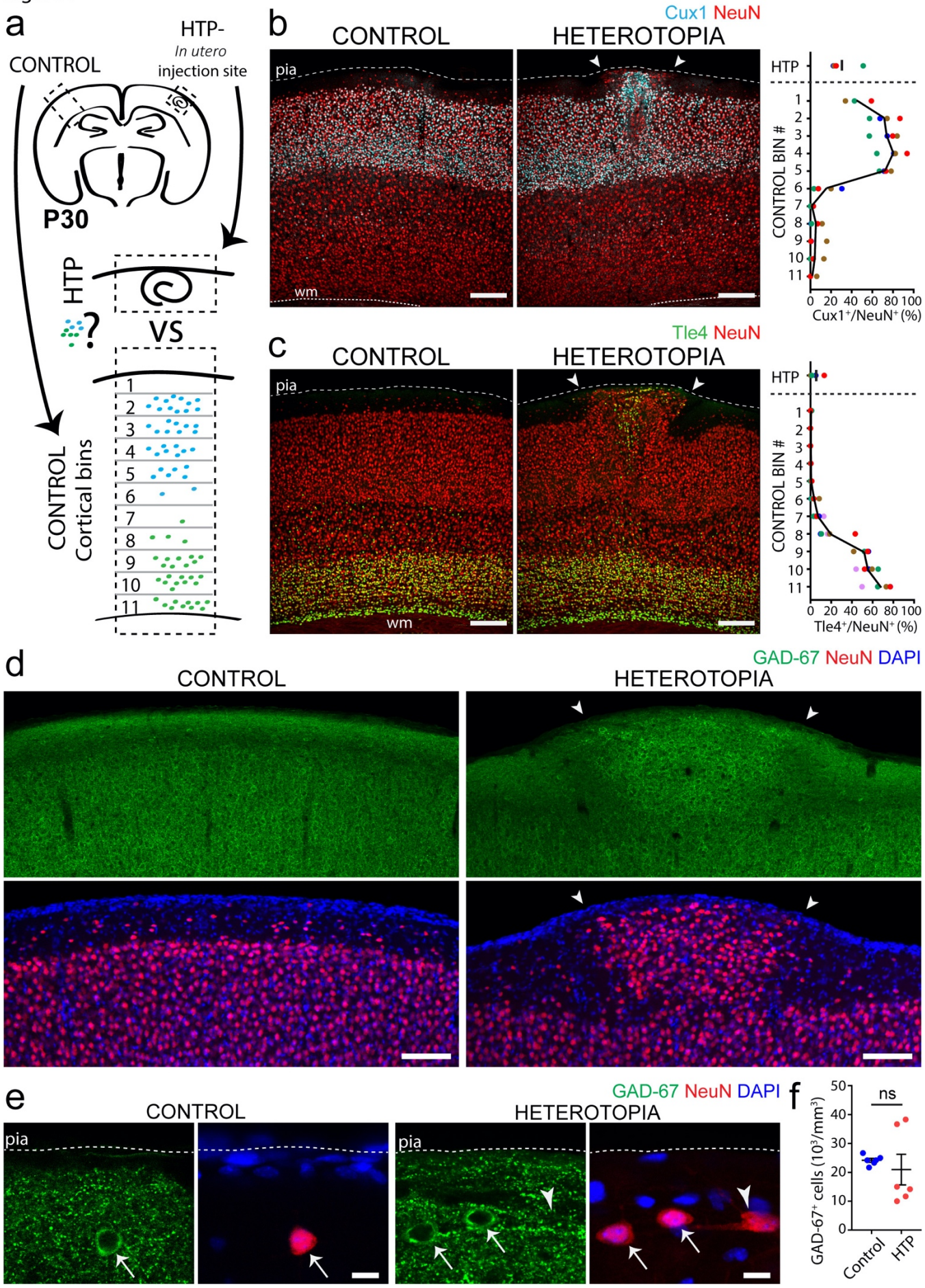
a
CONTROL
HTP-
In utero
injection site
P30
HTP
?
VS
CONTROL
Cortical bins
1
2
3
4
5
6
7
8
9
10
11
b
Cux1 NeuN
CONTROL
HETEROTOPIA
pia
wm
HTP
CONTROL BIN #
Cux1+/NeuN+ (%)
c
Tle4 NeuN
CONTROL
HETEROTOPIA
pia
wm
HTP
CONTROL BIN #
Tle4+/NeuN+ (%)
d
GAD-67 NeuN DAPI
CONTROL
HETEROTOPIA
e
GAD-67 NeuN DAPI
CONTROL
HETEROTOPIA
pia
pia
f
ns
GAD-67+ cells (10³/mm³)
Control
HTP

Figure 7–figure supplement 1

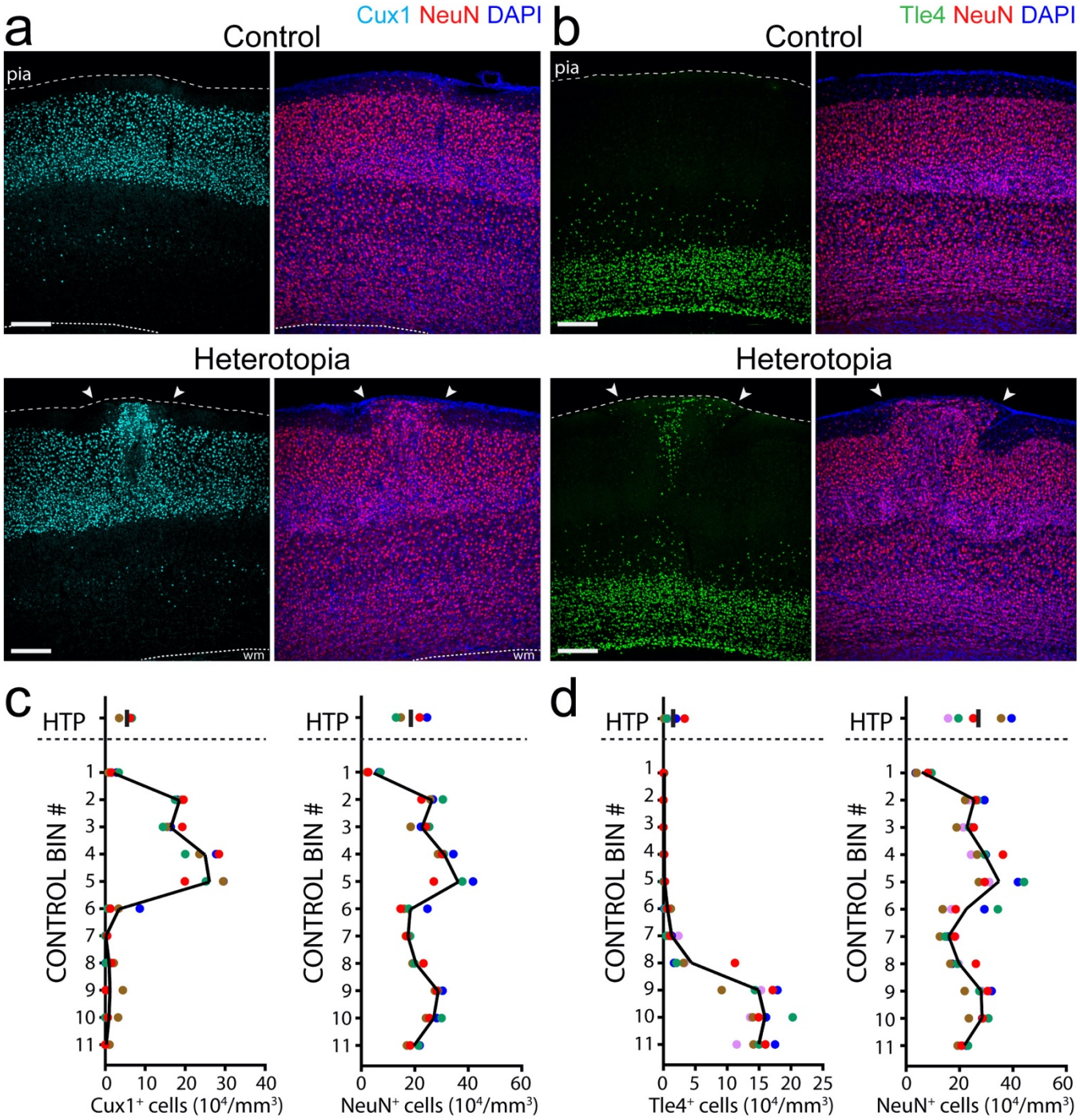

Figure 7–figure supplement 2

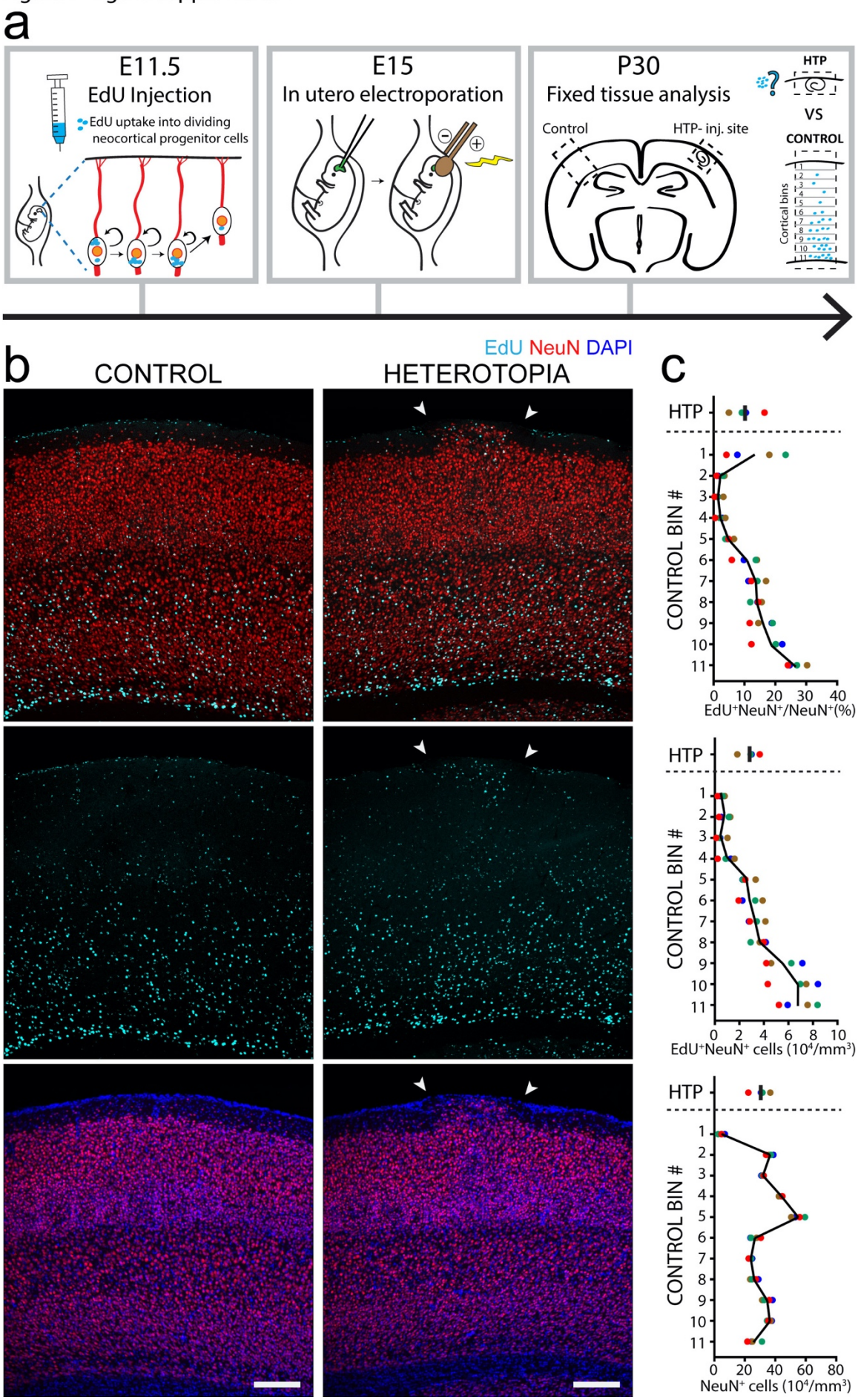

Figure 8

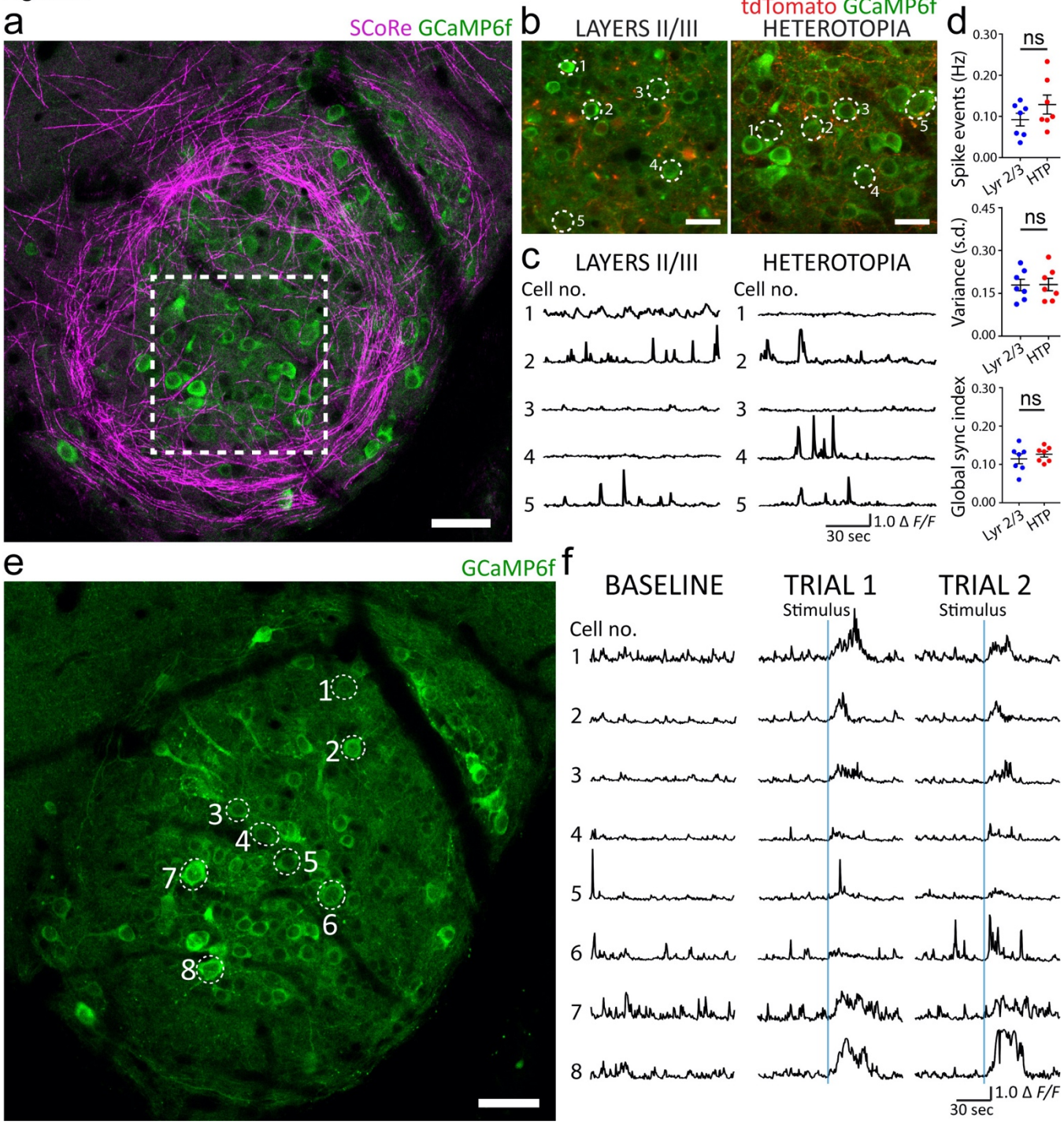
a
SCoRe GCaMP6f
b
LAYERS II/III
tdTomato GCaMP6f
HETEROTOPIA
c
LAYERS II/III
HETEROTOPIA
Cell no.
1.0 Δ F/F
30 sec
d
Spike events (Hz)
Variance (s.d.)
Global sync index
ns
Lyr 2/3
HTP
e
GCaMP6f
f
BASELINE
TRIAL 1
TRIAL 2
Stimulus
Cell no.
1.0 Δ F/F
30 sec

Supplementary Table 1					
Figure Number	**Statistical Test**	**Sample Size**	**Sample Definition**	**P Value**	**Degrees of Freedom and F/T/z/R/ETC value**
1b	Wilcoxon non-parametric matched-pairs signed rank test	6	number of mice (paired samples)	p = 0.0313 for NeuO, HTP vs. Control	n/a
2d	Wilcoxon non-parametric matched-pairs signed rank test	8	number of mice (paired samples)	SCoRe density, p=0.0078 for HTP edge vs. Control; p=0.0078 for HTP center vs. Control	n/a
	Wilcoxon non-parametric matched-pairs signed rank test	6	number of mice (paired samples)	p = 0.0313 for CNPase density, HTP vs. Control.	n/a
	Wilcoxon non-parametric matched-pairs signed rank test	6	number of mice (paired samples)	p = 0.0313 for CNPase$^+$ cell bodies, HTP vs. Control.	n/a
5c	Wilcoxon non-parametric matched-pairs signed rank test	6	number of mice (paired samples)	p > 0.9999 for CNPase$^+$ cell bodies, HTP vs. Control.	n/a
	Wilcoxon non-parametric matched-pairs signed rank test	6	number of mice (paired samples)	p = 0.0625 for CNPase density, HTP vs. Control.	n/a
6c	Wilcoxon non-parametric matched-pairs signed rank test	6	number of mice (paired samples)	p = 0.8438 for Aldh1L1$^+$ cell density, HTP vs. Control.	n/a
6f	Wilcoxon non-parametric matched-pairs signed rank test	6	number of mice (paired samples)	p = 0.9375 for Iba$^+$ cell density, HTP vs. Control	n/a
7f	Wilcoxon non-parametric matched-pairs signed rank test	6	number of mice (paired samples)	p = 0.5313 for GAD67$^+$ cell density, HTP vs Control	n/a
8d	Wilcoxon non-parametric matched-pairs signed rank test	7	number of mice (paired samples)	p = 0.6875 for spike event frequency, HTP vs Layers II/III	n/a
	Wilcoxon non-parametric matched-pairs signed rank test	7	number of mice (paired samples)	p = 0.9375 for variance (s.d.), HTP vs. Layers II/III	n/a
	Wilcoxon non-parametric matched-pairs signed rank test	7	number of mice (paired samples)	p = 0.2969 for global synchronization index, HTP vs. Layers II/III	n/a